Computational Mechanics (2025) 75:875–896
https://doi.org/10.1007/s00466-024-02536-7

ORIGINAL PAPER

Modeling cellular self-organization in strain-stiffening hydrogels

A. H. Erhardt[1] · D. Peschka[1] · C. Dazzi[2] · L. Schmeller[1] · A. Petersen[2,3] · S. Checa[2] · A. Münch[4] · B. Wagner[1]

Received: 3 May 2024 / Accepted: 1 August 2024 / Published online: 31 August 2024

Abstract

We derive a three-dimensional hydrogel model as a two-phase system of a fibre network and liquid solvent, where the nonlinear elastic network accounts for the strain-stiffening properties typically encountered in biological gels. We use this model to formulate free boundary value problems for a hydrogel layer that allows for swelling or contraction. We derive two-dimensional plain-strain and plain-stress approximations for thick and thin layers respectively, that are subject to external loads and serve as a minimal model for scaffolds for cell attachment and growth. For the collective evolution of the cells as they mechanically interact with the hydrogel layer, we couple it to an agent-based model that also accounts for the traction force exerted by each cell on the hydrogel sheet and other cells during migration. We develop a numerical algorithm for the coupled system and present results on the influence of strain-stiffening, layer geometry, external load and solvent in/outflux on the shape of the layers and on the cell patterns. In particular, we discuss alignment of cells and chain formation under varying conditions.

Keywords Hydrogels · Hyperelasticity · Nonlinear diffusion and reaction · Agent-based modeling · Cell migration

Mathematics Subject Classification 65Z05 · 74B05 · 74B20 · 92C10 · 92C17

1 Introduction

The development of hydrogel-based biomaterials as model systems for the extracellular matrix (ECM) is a promising approach for the discovery of new strategies for tissue engineering and regenerative medicine [1–4]. It enables a detailed understanding of the mechanical cell-cell interactions as well as mechanical interactions between individual cells and the surrounding ECM that will be important in biological processes such as tissue regeneration, angiogenesis, cancer and tissue morphogenesis in general [5–11].

Many tissues in the body, such as bone, cartilage, and the heart, are constantly subjected to mechanical loading that influences cell behavior. Experiments with hydrogel sheets that mimic ECM properties and apply physiological loading allow to investigate cell responses in controlled environments, advancing tissue engineering. Customizable hydro-

✉ A. H. Erhardt
andre.erhardt@wias-berlin.de

D. Peschka
dirk.peschka@wias-berlin.de

C. Dazzi
chiara.dazzi@charite.de

L. Schmeller
leonie.schmeller@wias-berlin.de

A. Petersen
ansgar.petersen@charite.de

S. Checa
sara.checa@charite.de

A. Münch
muench@maths.ox.ac.uk

B. Wagner
barbara.wagner@wias-berlin.de

[1] Weierstrass Institute, Mohrenstr. 39, 10117 Berlin, Germany

[2] Julius Wolff Institute, Berlin Institute of Health, Charité Universitätsmedizin, Augustenburger Platz 1, Berlin 13353, Germany

[3] BIH Center for Regenerative Therapies, Berlin Institute of Health, Charité Universitätsmedizin, Augustenburger Platz 1, 13353 Berlin, Germany

[4] Mathematical Institute, University of Oxford, Woodstock Road, Oxford OX2 6GG, UK

gels open new possibilities for delivering small molecules, proteins, and cells, and for tissue engineering, including self-healing, injectable hydrogels, and patches [12–14]. For instance, personalized heart patches can be created by combining ECM hydrogels, cardiomyocytes, and endothelial cells [15–18].

ECM materials can be experimentally characterized and mathematically modeled as viscoelastic hydrogels [19], i.e. a mixture of an elastic network and a solvent. In the past, hydrogels have been used in cell culture to study various cell functions, and to isolate mechanisms influencing cell migration [20]. Also, for comparison, stress–strain measurements can in principle be directly performed under stress- or strain-controlled conditions to distinguish between the elastic and viscous components. In addition, stress changes over time under a specific strain allow to infer details of hydrogel relaxation, which can give insights if traction forces applied by cells as they migrate lead to force or dissipation of the energy as a response [21–23].

It is known that cells migrate along stiffness gradients of the ECM. Typically, cells move towards a higher stiffness [24], while cases of migration towards softer regions has also been observed in vitro [25]. One mode of cell migration is initiated by the adhesion of a cell to the network fibers of the ECM, followed by the cell's polarization due to mechanical strains of the ECM accompanied by the cytoskeleton restructuring and elongation to initiate cell migration. The internally generated traction force applied by the cells results in a migration path that is either stochastic or follows directional migration paths, depending on various mechanical properties of the ECM [9, 26]. Moreover, while the strain they impose is strongest close to the cell and introduces locally a stiffness that can be many times higher than the applied stress, they also impact their surrounding region [27]. As shown in Liu et al. [28], cells, or even a single cell, may induce bands of fibers that lead to an increase in fiber density and alignment between cells. Such mechanical coupling between cells is suggested to be a universal mechanism in natural ECM and in particular collagen and fibrin gels [29, 30]. The strain-stiffening property is characteristic of the ECM and typical for natural hydrogels, i.e. composed of biomolecular networks, such as actin, collagen [30, 31], fibrin [29]. To some extent nonlinear stiffening has even been observed experimentally for stiff tissues such as cortical bones [32].

Mechanical properties of the extracellular matrix such as viscoelasticity and nonlinear elasticity directly affect cell migration, leading cells to restructure parts of their cytoskeleton [33, 34]. In turn, cells actively influence material properties of the extracellular matrix, such as stiffness, or actively remodel the network itself [35, 36], which in turn affects cell functions. This interaction between cells and the ECM is fundamental to understand tissue formation.

Agent-based cellular models coupled with finite element model describing the ECM are commonly utilized to model and investigate phenomena like bone regeneration, see [9, 11, 37, 38] and the references contained therein. Theoretical mechanical models and mechanisms for cell-hydrogel interactions are reviewed in [39]. General models for swelling hydrogels are considered in [40–43] and corresponding numerical schemes are developed in [44–46].

The goal of this study is the modeling and simulation of cell-hydrogel interaction. In addition, we will investigate how initial seedings of cells on the ECM evolve into self-organized cell patterns by taking into account the local and long-range mechanical interactions and solvent diffusion. To this end, we use an agent-based model in which discrete cells can be simulated to behave autonomously according to a set of rules. We will focus here on strain-stiffening properties by introducing a Gent-type model into our hydrogel model for the ECM. In this line of research, we study cell-hydrogel and cell-cell interactions for stretched and unstretched hydrogels, and we investigate the long-time evolution of an interacting cell system. The impact of mechanical ECM properties is investigated by comparing strain-stiffening Gent-type behavior and strain-softening neo-Hookean, where we also allow for solvent exchange with the surrounding. Performing a plane-strain or a plane-stress approximation, we study two effective 2D models for thin sheets or thick elastic layers.

The paper is structured as follows: In Sect. 2 we derive the mathematical model framework for the cells and the hydrogel, beginning with the derivation of a thermodynamically consistent continuum model for the hydrogel as a two-component system consisting of a nonlinearly elastic network in a liquid solvent in 3D in Sect. 2.1. We employ two different nonlinear elasticity models, a Gent-type and for comparison a neo-Hooke model. The former accounting for strain-stiffening properties of the fiber network. This is followed by the derivation of 2D approximations for hydrogel layers and specification of the fixed and free boundary conditions. We then introduce the agent-based model (ABM) in Sect. 2.3 to specify the migration rules and the iterative path of migration decisions by the cells when interacting with the hydrogel layer.

In Sect. 3 we investigate scenarios of hydrogel layers in 2D approximations for a range of applied external loads. This will lay the foundation for the cell-hydrogel interaction studies, which is necessary since the dynamic and morphological evolution of stretched hydrogel sheets has not been modeled before, at least not as a continuum multi-component free boundary system. We investigate stress–strain relations and the corresponding temporal and spatial evolution for different parameter configurations, different elasticity models, such as neo-Hooke or Gent, and different solvent concentrations, as well as the effects of possible solvent loss (or gain, i.e. swelling).

Finally, in Sect. 4 we explore the migration response of cell populations for various mechanical stimuli provided by the hydrogel sheet. Beginning with conditions without external load for hydrogel as well as pure elastic sheets, we vary the magnitude of the applied stretch, flux conditions at the free boundaries, strength of traction forces exerted by the cells. Following the evolution of the cell population we monitor corresponding pattern formation of the cells together with their orientation, distribution of solvent within the hydrogel sheet and the stress state. In particular, we explore conditions for chain formation of cells, that are well documented in the literature and discuss underlying mechanisms for their formation as well effects of strain stiffening. In Sect. 5 we conclude and discuss this work and future extensions of our model framework.

2 Model framework for cell-hydrogel interaction

In this section we develop a mathematical framework for viscoelastic hydrogels and combine them with an agent-based model as a minimal description of cell migration in an ECM and natural hydrogels. We derive a three-dimensional time-dependent continuum model for a hydrogel based on the thermodynamics of a two-component system consisting of cross-linked biopolymers and a solvent. We introduce a *Gent-type* model to capture the typical elastic properties of the network phase of natural hydrogels such as actin, fibrin or collagen, which typically exhibit strain-stiffening properties. As a limiting case we also consider the classical *neo-Hooke* model. Our model also accounts for possible solvent exchange with the environment via free boundaries to allow for contraction or swelling, reflecting typical in vitro experiments or the ECM. We then present a model reduction to two dimensions via the *plane-stress* approximation for thin hydrogel sheets, typically used in in vitro setups [9, 10], and for comparison also investigate the *plane-strain* approximation, relevant for thick layers. Finally, we introduce corresponding agent-based models for cell migration.

2.1 Hydrogel model

The dynamic hydrogel model is formulated in the Lagrangian frame $\Omega \subset \mathbb{R}^3$. The mechanical state of the hydrogel is characterized by a function $\boldsymbol{\chi} : [0,T] \times \Omega \to \mathbb{R}^3$, where $\boldsymbol{\chi}(t,\boldsymbol{x}) \in \mathbb{R}^3$ encodes the deformed position of a material point $\boldsymbol{x} \in \Omega$ at the time $t \in [0,T]$. With $\boldsymbol{F} = \nabla \boldsymbol{\chi} \in \mathbb{R}^{3\times 3}$ we denote the deformation gradient and with $J = \det(\boldsymbol{F})$ its determinant. The chemical state of the material is characterized by a concentration $\boldsymbol{c} : [0,T] \times \Omega \to \mathbb{R}^n$, where each component of $\boldsymbol{c} = (c_1, ..., c_n)$ encodes the concentration c_i of a component $i = 1,\dots,n$ for $n \in \mathbb{N}$ (i.e. the number of molecules of component i per unit volume in the Lagrangian frame Ω). Combining deformation and concentration into a state vector $\boldsymbol{q} = (\boldsymbol{\chi}, \boldsymbol{c})$ we have a free energy functional for the hydrogel

$$\mathscr{F}(\boldsymbol{q}) = \int_\Omega W(\boldsymbol{F}, \boldsymbol{c}, \nabla \boldsymbol{c}) - \boldsymbol{f} \cdot \boldsymbol{\chi} \, \mathrm{d}\boldsymbol{x}, \tag{1a}$$

$$W = W_{\text{mech}} + W_{\text{chem}}, \tag{1b}$$

where the density $W_{\text{mech}}(\boldsymbol{c}, \boldsymbol{F})$ contains the elastic stored energy of the hydrogel network and the density $W_{\text{chem}}(\boldsymbol{F}, \boldsymbol{c}, \nabla \boldsymbol{c})$ contains chemical and entropic contributions to the free energy that drive diffusion, phase transitions and phase separation and are therefore thermodynamic in nature. Additionally, with $\boldsymbol{f} : \Omega \to \mathbb{R}^3$ we encode given (external) mechanical forces. Each component takes up a certain volume fraction $\varphi_i = \alpha_i c_i / J$ with the component $\alpha_i > 0$ of the vector of specific molar volumes $\boldsymbol{\alpha} \in \mathbb{R}^n$. Setting

$$J = \sum_{i=1}^{n} \alpha_i c_i = 1 + \sum_{i=1}^{n-1} \alpha_i (c_i - \bar{c}_i) =: I(\boldsymbol{c}), \tag{2}$$

we have by construction $\sum_{i=1}^{n} \varphi_i = 1$. This definition of volume fractions and incompressibility is a generalization of the common definition in literature [43, 47, 48] to multicomponent systems. In the last step we assumed that c_n corresponding to the polymer network concentration is constant in space and time and that $J = 1$ in the reference state, where $c_i(t,\boldsymbol{x}) = \bar{c}_i$ for $i = 1, ..., n-1$ and $\boldsymbol{x} \in \Omega$. This constraint is enforced by a Lagrange multiplier $p : [0,T] \times \Omega \to \mathbb{R}$ contained in a state vector $\boldsymbol{q}_p = (\boldsymbol{q} = (\boldsymbol{\chi}, \boldsymbol{c}), p)$ using the Lagrangian

$$\mathscr{L}(\boldsymbol{q}_p) = \mathscr{F}(\boldsymbol{q}) + \int_\Omega p\Big(J - I(\boldsymbol{c})\Big) \, \mathrm{d}\boldsymbol{x}. \tag{3}$$

Minimizers of the free energy (1) subject to the incompressibility constraint (2) can be obtained by considering saddle points of the Lagrangian (3). Now, we construct a thermodynamic consistent evolution law for this system, i.e. the free energy is decreasing over time. Thus, we introduce chemical potential-like variables $\xi, \bar{\xi} : \Omega \to \mathbb{R}^n$ and construct the diffusive mobility of components

$$a(\xi, \bar{\xi}) = \int_\Omega \sum_{i,j=1}^{n-1} \sum_{k,l=1}^{d} \partial_{x_k} \xi_i : \boldsymbol{M}_{ik,jl} \, \partial_{x_l} \bar{\xi}_j \, \mathrm{d}\boldsymbol{x}.$$

In general, $\boldsymbol{M}(\boldsymbol{q})$ is a non-negative tensor that acts on components and spatial indices and depends on the concentration $\boldsymbol{c}$. A further dependence of $\boldsymbol{M}$ on $\boldsymbol{F}$ allows to include both anisotropic diffusion and Eulerian interfacial energies. The

corresponding diffusion is often diagonal in the concentration and with mobility function $m_i = m_i(c_i)$ leads to

$$a(\xi, \bar{\xi}) = \int_\Omega \sum_{i=1}^{n-1} m_i \, \nabla \xi_i \cdot \nabla \bar{\xi}_i \, \mathrm{d}\boldsymbol{x}. \tag{4}$$

Corresponding to the time derivative of the state $\partial_t \boldsymbol{q}_p = (\partial_t \boldsymbol{\chi}, \partial_t \boldsymbol{c}, \partial_t p)$ we consider general rates $\boldsymbol{w} = (\boldsymbol{w}_\chi, w_{\boldsymbol{c}}, w_p)$ with $\boldsymbol{w}_\chi : \Omega \to \mathbb{R}^3$, $w_{\boldsymbol{c}} : \Omega \to \mathbb{R}^n$ and $w_p : \Omega \to \mathbb{R}$ and define a bilinear form

$$b(\xi, \boldsymbol{w}) = \int_\Omega \xi \cdot w_{\boldsymbol{c}} \, \mathrm{d}\boldsymbol{x} \tag{5}$$

coupling chemical potentials $\eta : [0, T] \times \Omega \to \mathbb{R}^n$ and these rates. We model the evolution of the hydrogel by a nonlinear saddle point problem, where we seek $\boldsymbol{q}_p(t)$ and $\eta(t)$ such that

$$a(\eta(t), \xi) + b(\xi, \partial_t \boldsymbol{q}_p(t)) = 0 \tag{6a}$$

$$b(\eta(t), \boldsymbol{w}) = \langle \mathrm{D}\mathscr{L}(\boldsymbol{q}_p(t)), \boldsymbol{w} \rangle \tag{6b}$$

holds for all (test functions) $\boldsymbol{w}$ and ξ at time $t \in (0, T)$. Here, we introduced the (Gateaux) derivative of the Lagrangian functional

$$\langle \mathrm{D}\mathscr{L}(\boldsymbol{q}_p), \boldsymbol{w} \rangle = \lim_{h \to 0} \tfrac{1}{h} \left[\mathscr{L}(\boldsymbol{q}_p + h\boldsymbol{w}) - \mathscr{L}(\boldsymbol{q}) \right].$$

For details of the corresponding model derivation we refer to [43, 46].

Thermodynamic consistency holds for (6) in the sense that if we choose $\boldsymbol{w} = (\partial_t \boldsymbol{\chi}, \partial_t \boldsymbol{c}, 0)$ we get from (6b) that $\langle \mathrm{D}\mathscr{L}(\boldsymbol{q}_p), \boldsymbol{w} \rangle = \frac{\mathrm{d}}{\mathrm{d}t} \mathscr{F}(\boldsymbol{q}(t)) = b(\eta, \boldsymbol{w})$, where we used that the constraint (2) is satisfied. Testing the first equation (6a) with the chemical potential $\xi = \eta$ we obtain the final result

$$\tfrac{\mathrm{d}}{\mathrm{d}t} \mathscr{F}(\boldsymbol{q}(t)) = -a(\eta(t), \eta(t)) \leq 0, \tag{7}$$

where we used that $a(\xi, \xi) \geq 0$ holds by construction of a for any ξ, since we consider nonnegative $\boldsymbol{M}$ in (4). We supplement this problem with homogeneous natural boundary conditions for $\boldsymbol{c}$ on the entire boundary $\partial\Omega$. For the deformation we impose homogeneous natural boundary conditions on $\Gamma_N \subset \partial\Omega$ and inhomogeneous Dirichlet boundary conditions $\boldsymbol{\chi}(t, \boldsymbol{x}) = \boldsymbol{\chi}_\Gamma(t, \boldsymbol{x})$ for $\boldsymbol{x} \in \Gamma_D = \partial\Omega \setminus \Gamma_N$ and given $\boldsymbol{\chi}_\Gamma$. Note that (7) does not strictly hold for time-dependent inhomogeneous Dirichlet boundary conditions, since the elastic energy effectively depends explicitly on time. However, while the free energy might even increase, the model (6) is thermodynamic consistent, since the resulting first Piola-Kirchhoff stress tensor P and the chemical potentials η

$$\mathsf{P}(\boldsymbol{q}) = \partial_{\boldsymbol{F}} W + p J \boldsymbol{F}^{-T}, \tag{8a}$$

$$\boldsymbol{\eta} = \partial_{\boldsymbol{c}} W - \nabla \cdot \partial_{\nabla \boldsymbol{c}} W - \boldsymbol{\alpha} p, \tag{8b}$$

contain all fundamental cross-coupling effects. Note that we used $\partial_{\boldsymbol{F}} J = J \boldsymbol{F}^{-T}$. The corresponding Cauchy stress is obtained as $\boldsymbol{\sigma} = J^{-1} \mathsf{P} \boldsymbol{F}^T$. The resulting general hydrogel evolution is

$$\partial_t \boldsymbol{c} - \nabla \cdot (\boldsymbol{M}(\boldsymbol{q}) \nabla \boldsymbol{\eta}) = 0 \quad \text{in } (0, T) \times \Omega, \tag{9a}$$

$$-\nabla \cdot \mathsf{P}(\boldsymbol{q}) = \boldsymbol{f} \quad \text{in } (0, T) \times \Omega, \tag{9b}$$

with the constraint (2) and boundary conditions that represent no-flux of all components through the boundaries, stress-free and clamped conditions,

$$\boldsymbol{\nu} \cdot \boldsymbol{M} \nabla \boldsymbol{\eta} = 0 \quad \text{on } (0, T) \times (\Gamma_N \cup \Gamma_D), \tag{9c}$$

$$\mathsf{P}(\boldsymbol{q}) \boldsymbol{\nu} = 0 \quad \text{on } (0, T) \times \Gamma_N, \tag{9d}$$

$$\boldsymbol{\chi} = \boldsymbol{\chi}_\Gamma \quad \text{on } (0, T) \times \Gamma_D, \tag{9e}$$

respectively. Initial conditions are $c_i(t = 0, \boldsymbol{x}) = \bar{c}_i \in \mathbb{R}$ for $i = 1, ..., n-1$ and $\boldsymbol{\chi}_\Gamma(t = 0, \boldsymbol{x}) = \boldsymbol{x}$. Here $\boldsymbol{\nu}$ is the outer normal vector field on $\partial\Omega$. Alternatively to (9c), we also consider cases where solvent can flow into the gel through the free boundaries with a flux

$$\boldsymbol{\nu} \cdot \boldsymbol{M}(\boldsymbol{q}) \nabla \boldsymbol{\eta} = -n(\boldsymbol{q}) \boldsymbol{\eta}, \tag{10}$$

with some $n(\boldsymbol{q})$. In an effective 2D model for a thin sheet will lead to volumetric source terms in the hydrogel model. We assume that the system is initially in equilibrium, i.e. $\mathscr{F}$ is minimal for $\boldsymbol{F} = \mathbb{I}$, $\boldsymbol{c} = \bar{\boldsymbol{c}}$ and $p = 0$ for $\boldsymbol{f} = 0$. Next, we specify the energy density and restrict to two components, i.e. $n = 2$, for solvent and elastic polymer molecules. In order to investigate the impact that the solvent diffusion has on the gel dynamics, we want to be able to revert the model to a simple hyperelastic model. This can be achieved by switching off the diffusion setting $\boldsymbol{M} = 0$ and thus $\boldsymbol{c} = \bar{\boldsymbol{c}}$ and $J = 1$ for all times. In the following we explain specific choices for the energy density that reflect the expected mechanical and thermodynamic properties of hydrogels.

Entropic energy density.

The energy density W_{chem} in (1) contains chemical and entropic contributions of thermodynamic origin that contribute to the free energy. We use here a Flory-Huggins free energy [49–51] expressed using gradients of the concentra-

tion and using volume fractions as

$$W_{\text{chem}}(\boldsymbol{F}, \boldsymbol{c}, \nabla \boldsymbol{c}) = \Big(\tfrac{1}{2}\nabla \boldsymbol{c} : \boldsymbol{\gamma}(\boldsymbol{F})\nabla \boldsymbol{c} + k_0 + \sum_{i=1}^{n} k_i \varphi_i \ln(\varphi_i) + \sum_{j>i} \chi_{ij}\varphi_i\varphi_j\Big) J, \tag{11}$$

which describes the mixing of the polymeric system [43], where $\boldsymbol{\gamma}$ plays the role of a surface energy. Here, we restrict to a binary mixture with $n = 2$, where $\boldsymbol{c} = (c_1, c_2)$ and denote for $c := c_1$, similarly, $\bar{c} := \bar{c}_1$, $\alpha := \alpha_1$, $\varphi_1 := \varphi$ and $\varphi_2 := 1-\varphi$ so that the parameters in the density reduce to $\boldsymbol{\gamma}$, three constants k_0, k_1, k_2 and the mixing parameter χ_{12} such that

$$W_{\text{chem}} = \Big[\tfrac{\gamma}{2}|\nabla c|^2 + k_0 + k_1\varphi\ln(\varphi) + k_2(1-\varphi)\ln(1-\varphi) + \chi_{12}\varphi(1-\varphi)\Big] J, \tag{12}$$

with $\varphi = \alpha c/J$. Depending on the sign of the mixing parameter χ_{12} one can trigger whether mixing or phase separation is energetically favorable. In the following we assume $\chi_{12} = 0$. While $k_1, k_2 > 0$ can be chosen arbitrarily and $\partial_{\boldsymbol{F}} W_{\text{mech}}(\bar{c}, \mathbb{I}) = 0$ see Fig. 1, we set k_0 so that $\partial_{\boldsymbol{F}} W_{\text{chem}} = 0$ in equilibrium, i.e. $c = \bar{c}$ and $\boldsymbol{F} = \mathbb{I}$. Therefore, the material is stress-free in the prepared reference state. In [44] a similar constant k_0 was used to ensure existence of minimizers by ensuring $W_{\text{chem}}(\boldsymbol{F}, \boldsymbol{c}, \nabla \boldsymbol{c}) \geq 0$ for all $\det \boldsymbol{F} \geq 0$.

Elastic energy density.

For this study we use neo-Hookean elastic materials as one of the simplest nonlinear elasticity models, or alternatively a Gent-type material that accounts for the strain-stiffening properties of a hydrogel. Therefore, in the following we introduce elastic energy densities $W_{\text{mech}}(\boldsymbol{c}, \boldsymbol{F}) = W^i_{\text{mech}}(\boldsymbol{c}, \boldsymbol{F})$ which allows us to investigate properties of strain-softening by a neo-Hookean energy $i =$ "neo-Hooke" or strain-stiffening by a Gent-type energy $i =$ "Gent". These nonlinear material models for large deformations contrast a simple linear elastic model typically valid only for small deformations, see Fig. 1.

Commonly used constitutive material laws for describing the nonlinear elastic response of a polymer network are of *neo-Hookean* type [52]. Here, the strain energy density is given by

$$W^{\text{neo-Hooke}}_{\text{mech}} = \frac{\mu}{2}\left(\text{tr}(\mathbb{C} - \mathbb{I}) - 2\ln(J)\right) \tag{13}$$

with $J = \sqrt{\det(\mathbb{C})}$ and left Cauchy–Green tensor $\mathbb{C} = \boldsymbol{F}^T\boldsymbol{F}$. Compared to a linear elastic material, the stress–strain relation also starts linear but will flatten for larger strains.

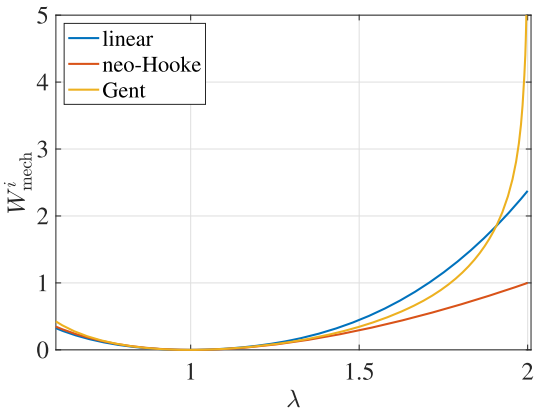

Fig. 1 Mechanical energy density with $\mu = 1$ for linear elastic material, neo-Hooke and Gent model ($J_m = 2$) for the deformation in (15). The 3D Gent model becomes singular at $\lambda = 2$

We model strain stiffening hydrogels by employing the *Gent model* [53] with strain energy

$$W^{\text{Gent}}_{\text{mech}} = -\frac{\mu}{2}\left(J_m \ln\left(1 - \tfrac{1}{J_m}\text{tr}(\mathbb{C} - \mathbb{I})\right) + 2\ln(J)\right), \tag{14}$$

where $J_m = I_m - 3$ is the so-called limiting deformation of the material, $I_1 = \text{tr}(\mathbb{C})$ is the first invariant of the right Cauchy-Green deformation tensor and I_m is the limiting value of I_1. Stretchability of soft tissue varies with age, pathology, humidity, as well as the type of tissue [54]. Tendons and ligaments can be uniaxially stretched to a strain of around 15% [55], cartilage 120% [55], skins 110% [56] and aorta 100% [55]. These value correspond to a deformation $J_m = 0.06, 2.75, 2.36$ and 2.00, respectively. This parameter can be tuned by changing the cross-link density of the polymer chains or by varying the mixture of different kinds of polymers. In the limit $I_m \to \infty$ the Gent model converges to the neo-Hookean model. In Fig. 1 we show the three elastic energy densities for a uniaxial deformation with $J = 1$ of the form

$$\boldsymbol{F} = \begin{pmatrix} \lambda & 0 & 0 \\ 0 & \lambda^{-1/2} & 0 \\ 0 & 0 & \lambda^{-1/2} \end{pmatrix}, \tag{15}$$

showing clearly that the energies W^i_{mech} are minimal for $\boldsymbol{F} = \mathbb{I}$ and that Gent or neo-Hookean materials are softer or stiffer compared to linear elastic ones for larger strains λ, respectively. For elastic models one might want to consider a dependence $\mu = \mu(\boldsymbol{c})$ to describe the effect of drying-induced softening or stiffening as in [57], but here we will consider a constant elastic modulus that does not depend on concentration.

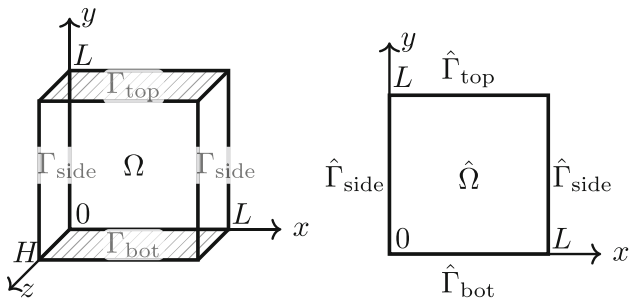

Fig. 2 (left) 3D sheet $\Omega = \hat{\Omega} \times (0, H)$ and (right) its 2D cross section $\hat{\Omega} = (0, L)^2$. We denote the top and bottom faces of the cuboid by $\Gamma_{\text{top}} = \hat{\Gamma}_{\text{top}} \times (0, H)$ and $\Gamma_{\text{bot}} = \hat{\Gamma}_{\text{bot}} \times (0, H)$ where $\hat{\Gamma}_{\text{top}} = (0, L) \times \{L\}$ and $\hat{\Gamma}_{\text{bot}} = (0, L) \times \{0\}$, as indicated by the gray dashed lines. The side faces of the cuboid are $\Gamma_{\text{side}} = \hat{\Gamma}_{\text{side}} \times (0, H)$ where $\hat{\Gamma}_{\text{side}} = \{0, L\} \times (0, L)$. Additionally, the front faces of the cuboid are $\Gamma_{\text{front}} = (0, L)^2 \times \{0, H\}$

2.2 Reduction to two dimensions

We consider an elastic sheet in a rectangular cuboid domain $\Omega = \hat{\Omega} \times (0, H) \subset \mathbb{R}^3$ with $\hat{\Omega} = (0, L)^2$ with the simple sheet geometry shown in Fig. 2. In that sketch we introduce front, side, top and bottom faces on which boundary conditions are defined. In order to solve (9) we use inhomogeneous Dirichlet boundary conditions on $\Gamma_D = \Gamma_{\text{top}} \cup \Gamma_{\text{bot}}$ and no-stress boundary conditions on $\Gamma_N = \Gamma_{\text{side}} \cup \Gamma_{\text{front}}$.

Model reduction for elastic sheets and membranes is usually based on an assumption that a general elastic deformation $\boldsymbol{\chi}(t, \boldsymbol{x}) = \boldsymbol{x} + \boldsymbol{u}(t, \boldsymbol{x})$ depending on time t and space $\boldsymbol{x} = (\hat{x}, z)$ with $\hat{x} = (x, y)$. Notice that we print two-dimensional vectors in normal font, while boldface continues to be used for higher-dimensional vectors and for tensors. The displacement $\boldsymbol{u}(t, \boldsymbol{x})$ can be approximated by

$$\boldsymbol{u}(t, \boldsymbol{x}) = \begin{pmatrix} \hat{u}_x(t, \hat{x}) \\ \hat{u}_y(t, \hat{x}) \\ \hat{w}(t, \hat{x})(z - \frac{H}{2}) \end{pmatrix},$$

with functions $\hat{u}_x, \hat{u}_y, \hat{w} : [0, T] \times \hat{\Omega} \to \mathbb{R}$ that only depend on the cross-section $\hat{\Omega}$ and thus

$$\boldsymbol{F} = \begin{pmatrix} \hat{\boldsymbol{F}} & 0 \\ 0 & \hat{F}_{zz} \end{pmatrix}, \quad \hat{\boldsymbol{F}} = \begin{pmatrix} \hat{F}_{xx} & \hat{F}_{xy} \\ \hat{F}_{yx} & \hat{F}_{yy} \end{pmatrix}. \tag{16}$$

Notice that we also approximate the solvent concentration by $c(t, \boldsymbol{x}) = \hat{c}(t, \hat{x})$. Then we have for the determinant $\hat{J} \equiv \det \hat{\boldsymbol{F}}$ that

$$\hat{J} \hat{F}_{zz} = J = I(\hat{c}). \tag{17}$$

Under these assumptions one distinguishes the plane-stress approximation for thin sheets $H \ll L$ and the plane-strain approximation for thick layers, i.e. $H \gg L$.

Plane stress approximation.

Solving the condition (17) for a general $\hat{F}_{zz}$ with $I(c) = 1 + \alpha(\hat{c} - \bar{c})$ given by the constraint (2) yields an explicit expression

$$\hat{F}_{zz}(\hat{\boldsymbol{F}}, \hat{c}) = \frac{(1 + \alpha(\hat{c} - \bar{c}))}{\hat{J}}. \tag{18}$$

This allows to approximate the original three-dimensional problem by a two-dimensional problem for $\hat{\chi}(t, \hat{x}) = \hat{x} + \hat{u}(t, \hat{x}) \in \mathbb{R}^2$ where we use $\hat{u} = (\hat{u}_x, \hat{u}_y)$ and with $\hat{\boldsymbol{F}} = \nabla \hat{\chi}$ we can replace $\boldsymbol{F} = \boldsymbol{F}_{\text{stress}}(\hat{\boldsymbol{F}}, \hat{c})$ via (16) and (18) in the free energy. This approximation is commonly used for thin sheets $H \ll L$ with appropriate boundary conditions, e.g. here we are going to use $u_x = u_z = 0$ and $u_y = u_y^D$ on Γ_D for the 3D model or correspondingly $\hat{u}_x = 0$ and $\hat{u}_y = \hat{u}_y^D$ on $\hat{\Gamma}_D$ for the corresponding plane stress approximation. Note that in the plane stress approximation the constraint (2) is automatically satisfied and no multiplier is required. Thus, the plane stress approximation of a 3D incompressible material is effectively a 2D model that allows for compression in the xy-plane.

Plane strain approximation.

The corresponding plane strain approximation assumes $\hat{w} = 1$ and thus

$$\hat{F}_{zz} = 1. \tag{19}$$

This implies $J = \hat{J}$, so that the condition (2) becomes

$$\hat{J} = 1 + \alpha(\hat{c} - \bar{c}). \tag{20}$$

As in the 3D model, this condition is explicitly enforced using a Lagrange multiplier, see (22). Also this yields $\boldsymbol{F} = \boldsymbol{F}_{\text{strain}}(\hat{\boldsymbol{F}}, \hat{c})$ that can be used in the free energy and is here trivially independent of $\hat{c}$. This approximation is commonly used for $H \gg L$ or with appropriate boundary conditions on Γ_{front}. Thus, the plane strain approximation of a 3D incompressible material is effectively a 2D model that also does not allow for compression in the xy-plane.

Resulting 2D models.

The main step of both approximations is to replace the energy in (1) by the 2D approximation $\hat{\boldsymbol{q}} = (\hat{\chi}, \hat{c})$ for two-dimensional external forcing $\boldsymbol{f}(\boldsymbol{x}) = (\hat{f}(\hat{x}), 0)$, which gives

$$\hat{\mathscr{F}}(\hat{\boldsymbol{q}}) = \int_{\hat{\Omega}} W(\boldsymbol{F}_j(\hat{\boldsymbol{F}}, \hat{c}), \hat{c}, \hat{\nabla} \hat{c}) - \hat{f} \cdot \hat{\chi} \, \mathrm{d}\hat{x}, \tag{21}$$

where $W = W_{\text{mech}} + W_{\text{chem}}$ as before. We have also defined (from (16))

$$\boldsymbol{F}_j(\hat{\boldsymbol{F}}, \hat{c}) = \begin{pmatrix} \hat{\boldsymbol{F}} & 0 \\ 0 & \hat{F}_{zz} \end{pmatrix}$$

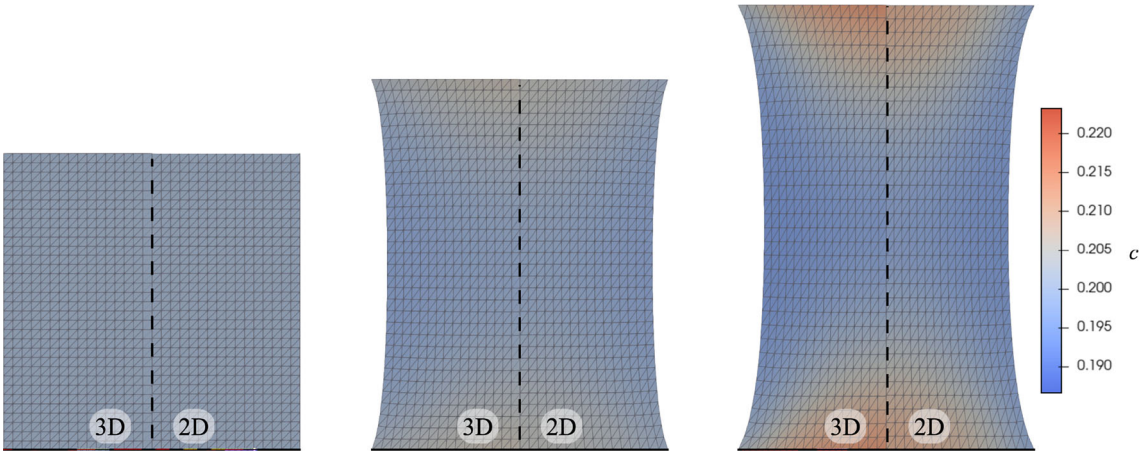

Fig. 3 Comparison of the cross-section of the 3D hydrogel model with the corresponding 2D hydrogel model in plane stress approximation (Gent). We show the deformed domain $\hat{\chi}(\hat{\Omega})$ (mesh) and the concentration $\hat{c}$ (shading) for increasing applied strain from left to right. The left half of each plot is from the 3D problem and the right half from the effective 2D problem

where for j = "stress", $\hat{F}_{zz}$ is replaced by (18) and for j = "strain" by (19). Note that, while in the plane stress approximation $\hat{\boldsymbol{q}}$ already satisfies the constraint (2), in the plane strain approximation we need to enforce it in the form (20) via a Lagrange multiplier p by defining the Lagrange functional

$$\hat{\mathscr{L}}(\hat{\boldsymbol{q}}_p) = \hat{\mathscr{F}}(\hat{\boldsymbol{q}}) + \int_{\hat{\Omega}} \hat{p}\big(\hat{J} - [1 + \alpha(\hat{c} - \bar{c})]\big)\mathrm{d}\hat{x}, \tag{22}$$

and using and augmented set of variables $\hat{\boldsymbol{q}}_p = (\hat{\boldsymbol{q}}, \hat{p})$. The bilinear forms for the effective 2D model are

$$\hat{a}(\xi, \bar{\xi}) = \int_{\hat{\Omega}} m(\hat{c})\, \hat{\nabla}\xi \cdot \hat{\nabla}\bar{\xi} + n(\hat{c})\xi\bar{\xi}\, \mathrm{d}\hat{x}. \tag{23}$$

and with rates $\boldsymbol{w} = (w_{\boldsymbol{\chi}}, w_c)$ for plane stress or $\boldsymbol{w} = (w_{\boldsymbol{\chi}}, w_c, w_p)$ for plane strain let

$$\hat{b}(\xi, \boldsymbol{w}) = \int_{\hat{\Omega}} \xi w_c\, \mathrm{d}\hat{x}, \tag{24}$$

where we avoided the "hats" on chemical potentials and rates for ease of notation. This choice of $\hat{a}$ leads to a model that combines dissipative effects of Cahn-Hilliard and Allen-Cahn models and thereby introduces conservative nonlinear diffusion and nonconservative nonlinear reaction in the hydrogel. The coefficient $n(\hat{c})$ in (23) takes into account the possible flux of solvent through the free boundaries that was introduced into the 3D model in (10) and can entail contraction and swelling of the material. Introducing a time discretization $\hat{\boldsymbol{q}}^k = \hat{\boldsymbol{q}}(k\tau)$ with time step size τ, in the plane stress approximation this leads to

$$\hat{a}(\eta^k, \xi) + \hat{b}(\xi, \delta_t \hat{\boldsymbol{q}}^k) = 0 \tag{25a}$$

$$\hat{b}(\eta^k, \boldsymbol{w}) = \langle \mathrm{D}\hat{\mathscr{F}}(\hat{\boldsymbol{q}}^k), \boldsymbol{w}\rangle \tag{25b}$$

with $\delta_t \hat{\boldsymbol{q}}^k = \frac{1}{\tau}(\hat{\boldsymbol{q}}^k - \hat{\boldsymbol{q}}^{k-1})$ and in the plane strain approximation with

$$\hat{a}(\eta^k, \xi) + \hat{b}(\xi, \delta_t \hat{\boldsymbol{q}}_p^k) = 0 \tag{26a}$$

$$\hat{b}(\eta^k, \boldsymbol{w}) = \langle \mathrm{D}\hat{\mathscr{L}}(\hat{\boldsymbol{q}}_p^k), \boldsymbol{w}\rangle. \tag{26b}$$

with $\delta_t \hat{\boldsymbol{q}}_p^k = \frac{1}{\tau}(\hat{\boldsymbol{q}}_p^k - \hat{\boldsymbol{q}}^{k-1})$. As described in [46], this nonlinear saddle point problem is discretized in space using finite elements on triangular meshes and discretized in time via an incremental minimization. We implement the problem using the finite element library FEniCS [58, 59]. Solving (25) or (26) with a force $\hat{f}$ produced by the cell configuration contributes to one time step (iteration) of the hydrogel model. For more details we also refer to the supplementary source code [60]. For thin sheets, a comparison of 2D and 3D deformation and concentration in the plane stress approximation in shown in Fig. 3. While in particular close to the top and bottom boundary, due to a mismatch of boundary conditions in the plane stress approximation slight differences in the solvent concentration are visible. Nevertheless, the 2D deformation describes the thin 3D hydrogel sheet very well. In the following we explain the ABM and the construction of the force $\hat{f}$ that couples to the hydrogel.

2.3 ABM for cell migration

For the interaction of the cells with the hydrogel we neglect the short time adhesion process and focus on the nonlinear

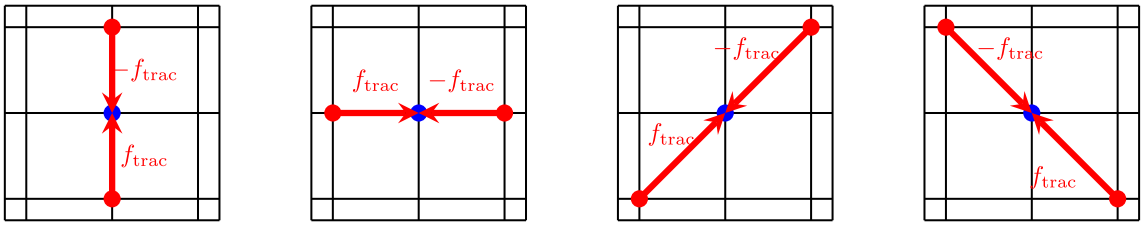

Fig. 4 Traction forces with a magnitude f_{trac} on the ECM induced by the cell (blue dot)

Table 1 Implementation of ABM that computes $\boldsymbol{a}(t^{k+1}) = \boldsymbol{a}^{k+1}$ and $\hat{\boldsymbol{q}}(t^{k+1}) = \hat{\boldsymbol{q}}^{k+1}$ based on the solution at previous time $t^k = k\tau$

1. Seed cell configuration	For the given $N = 100$ and $n_{\text{cells}} = 500$, initialize the multi-cell configuration by picking a random (iid) element $\boldsymbol{a}^0 \in \boldsymbol{A}$ and set $k = 0$. Set hydrogel initial data $\hat{\boldsymbol{q}}^0 = (\hat{\chi}^0 = \hat{x}, \hat{c} = \bar{c})$ at $t^0 = 0$
2. Propose cell update $\boldsymbol{a}^k \to \boldsymbol{a}^*$	For given $\boldsymbol{a}^k$, randomly select the cells $i \in I$ that will be updated (about 80% of the total population). Then select a random neighboring multi-cell state $\boldsymbol{a}^* \in \boldsymbol{A}$ where $a_i = a_i^*$ for $i \notin I$
3. Propose hydrogel update $\hat{\boldsymbol{q}}^*$	
a) Traction forces	Compute traction forces $\hat{f}(\boldsymbol{a}^*)$ by cells, cf. (28)
b) Boundary conditions	Apply inhomogeneous Dirichlet boundary conditions $\boldsymbol{\chi}_\Gamma(t = k\tau)$
c) Propose hydrogel state	Starting from $\hat{\boldsymbol{q}}^k$, find the tentative solution $\hat{\boldsymbol{q}}^*$ of the nonlinear hydrogel problem (25) or (26) at time $t^{k+1} = (k+1)\tau$ with traction from 3a)
4. Generate update $\boldsymbol{a}^{k+1}$	Cycle through all cells $1 \le i \le n_{\text{cells}}$ and perform 4a,b) to update cells
a) Deformation	Compare the new deformation $\text{def}(\hat{\boldsymbol{q}}^*, a_i^*)$ with the old $\text{def}(\hat{\boldsymbol{q}}^k, a_i^k)$ cf. (29)
b) Update	If the old deformation was lower and the old position $\hat{x}_i^k$ is unoccupied in $\boldsymbol{a}^*$, then $a_i^{k+1} = a_i^k$. Otherwise accept the update and set $a_i^{k+1} = a_i^*$
5. Generate update $\hat{\boldsymbol{q}}^{k+1}$	Compute hydrogel state based on updated cell states
a) Traction forces	Compute traction forces by cells $\hat{f}(\boldsymbol{a}^{k+1})$
b) Update hydrogel state	Starting from $\hat{\boldsymbol{q}}^k$, find the solution $\hat{\boldsymbol{q}}^{k+1}$ of the nonlinear hydrogel problem (25) or (26) at time $t^{k+1} = (k+1)\tau$ with traction from 5a)
6. Iterate	Set $t = (k+1)\tau$ and increment $k \to k+1$. Repeat steps 2.-6. until $t = T$

The update is performed via intermediate states for cells $\boldsymbol{a}^*$ and for hydrogel $\hat{\boldsymbol{q}}^*$. We say two single cells $a = (\hat{x}, d), a^* = (\hat{x}^*, d^*) \in A$ are *neighbors* and write $a \sim a^*$ if there exists a direction $\tilde{d} \in \Delta$ such that $\hat{x} = \hat{x}^* + \tilde{d}$ or $\hat{x} = \hat{x}^* - \tilde{d}$ or if $a = a^*$. Two multi-cell configurations $\boldsymbol{a}, \boldsymbol{a}^* \in \boldsymbol{A}$ are *neighbors* and we write $\boldsymbol{a} \sim \boldsymbol{a}^*$, if all of their components are neighbors $a_i \sim a_i^*$ for $i = 1, \dots, n_{\text{cells}}$. We say a cell position $\hat{x} \in \Omega_{\text{cell}}$ in $\boldsymbol{a} = (a_1, \dots, a_{n_{\text{cells}}}) \in \boldsymbol{A}$ is *unoccupied* (by a cell), if for no component $a_i = (\hat{x}_i, d_i)$ $i = 1, \dots, n_{\text{cells}}$ we have $\hat{x} = \hat{x}_i$. Otherwise we say the position $\hat{x}$ is *occupied* (by a cell) in $\boldsymbol{a}$

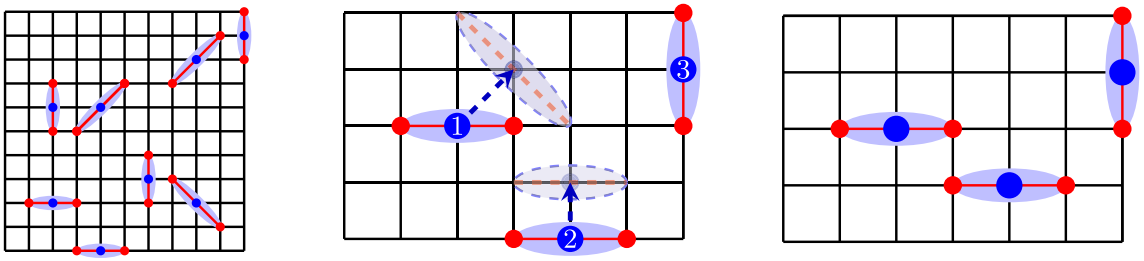

Fig. 5 (left) Exemplary multi-cell state $\boldsymbol{a} = (a_1, \dots, a_{n_{\text{cells}}}) \in \boldsymbol{A}$ for a lattice of cell position Ω_{cell} with $N = 10$ and $n_{\text{cells}} = 8$ and $a_i = (\hat{x}_i, d_i) \in A$. The cell center positions $\hat{x}_i$ are indicated using blue dots and the corresponding orientations d_i are indicated using red dots at $\hat{x}_i \pm d_i$ and red lines connecting these with the cell center. For any given state $\boldsymbol{a}$, the traction force $\hat{f}(\boldsymbol{a})$ pulls the hydrogel at each red dot towards the corresponding cell center with strength f_{trac}. (middle) Proposed cell update for the cell state from the bottom left corner of the multi-cell state. The new positions and orientations for cell 1 and cell 2 (white labels) are indicated using light blue dots and dashed blue lines, whereas cell 3 is fixed because at every iteration not all cells are updated. (right) New configuration where the updated cell state was rejected for cell 1 and accepted for cell 2

mechanics occurring on the time-scales of cell migration. Migrating cells are treated as having elongated shapes (spindle-like shape) with a spatial location and orientation. Each cell probes the hydrogel by exerting a dipole-like traction force of a given strength towards its center that is transmitted to the hydrogel and in turn to other cells, which are also probing the hydrogel. These properties of cells are described by a number of sets and functions, which we introduce next. The collective migration for a given distribution of cells is then described by an ABM (inspired by [9]) governing the migration decisions of each cell as a function of the states of other cells and the hydrogel. In our current study we restrict the investigation to capturing a basic property that is generally thought to govern cell migration, namely that cells prefer locations with higher stiffness [61]. Note that the migration speed of fibroblasts similar to the cells contained in the model is in the order of tens of microns per hour in vitro, see e.g. [62–64] for cells of typical size $\sim 50\mu$m and thus typical time scales of hours.

Cell state space.

First, we define the set of admissible states A of a single cell $a \in A$ and then the set of admissible states $\boldsymbol{A}$ of many cells $\boldsymbol{a} = (a_1, \dots, a_{n_{\text{cells}}})$ with $a_i \in A$ and $n_{\text{cells}} \in \mathbb{N}$. For the former, we assume that the cells can occupy positions on an $N \times N$ lattice Ω_{cell} with given $N \in \mathbb{N}$ and mesh size $h = L/N$ that spans the sheet (in the reference system),

$$\Omega_{\text{cell}} = \hat{\Omega} \cap (h\mathbb{Z})^2. \tag{27a}$$

In contrast to [9], we allow for four instead of two possible orientations, namely

$$\Delta = \left\{ d_{\leftrightarrow}, d_{\updownarrow}, d_{\swarrow}, d_{\searrow} \right\} \subset \mathbb{R}^2, \tag{27b}$$

where $d_{\leftrightarrow} = (h, 0)$, $d_{\updownarrow} = (0, h)$, $d_{\swarrow} = (h, h)$ and $d_{\searrow} = (h, -h)$. Then, the set of admissible states $(\hat{x}, d)$ is given by

$$A = \left\{ (\hat{x}, d) \in \Omega_{\text{cell}} \times \Delta \;\middle|\; \begin{array}{c} (d = d_{\updownarrow} \text{ if } \hat{x} \in \hat{\Gamma}_{\text{side}}) \\ \text{and} \\ (d = d_{\leftrightarrow} \text{ if} \hat{x} \in \hat{\Gamma}_{\text{top}} \cup \hat{\Gamma}_{\text{bot}}) \end{array} \right\}.$$

Notice that cells on the boundary are required to be aligned tangentially with the boundary. From this we construct the set of multi-cell configurations with $n_{\text{cells}} \in \mathbb{N}$ cells by

$$\boldsymbol{A} = \left\{ \left(a_1, \dots, a_{n_{\text{cells}}}\right) \in A^{n_{\text{cells}}} \mid \forall i \neq j : \hat{x}_i \neq \hat{x}_j \right\},$$

i.e. cells cannot occupy the same node.

The cells generate a dipole-type force $\hat{f}(\boldsymbol{a})$ that pulls material towards the cell center by pulling in the direction given by the cell orientation. For any cell configuration $\boldsymbol{a} = (a_1, \dots, a_{n_{\text{cells}}}) \in \boldsymbol{A}$ that force is

$$\hat{f}(\boldsymbol{a}) = \sum_{i=1}^{n_{\text{cells}}} \left(\delta_{\hat{x}_i - d_i} - \delta_{\hat{x}_i + d_i} \right) \frac{d_i}{\|d_i\|} f_{\text{trac}}, \tag{28}$$

where δ_x denotes the Dirac δ distribution and the traction strength is $f_{\text{trac}} > 0$, see also Fig. 4. For any given state of the hydrogel $\hat{\boldsymbol{q}} = (\hat{\chi}, \hat{c}) \in \hat{\boldsymbol{Q}}$, a single cell $a = (\hat{x}, d) \in A$ in the ABM can probe the response generated by the traction force by the function $\text{def} : \hat{\boldsymbol{Q}} \times A \to \mathbb{R}$ that measures the local deformation at the cell location $\hat{x} \in \Omega_{\text{cell}} \subset \mathbb{R}^2$ via

$$\text{def}(\hat{\boldsymbol{q}}, a) = \begin{cases} |\hat{u}_x(\hat{x} - d) - \hat{u}_x(\hat{x} + d)| & d = d_{\leftrightarrow} \\ |\hat{u}_y(\hat{x} - d) - \hat{u}_y(\hat{x} + d)| & d = d_{\updownarrow} \\ \|\hat{u}(\hat{x} - d) - \hat{u}(\hat{x} + d)\| & \text{else} \end{cases} \tag{29}$$

with $\|\hat{u}\| = (\hat{u}_x^2 + \hat{u}_y^2)^{1/2}$ and where $\hat{u} = (\hat{u}_x, \hat{u}_y)$. This function does not explicitly depend on $\hat{c}$.

Multi-cell update

The final modeling step is a description of the cell migration via an ABM satisfying certain rules [9, 10, 65, 66]. After seeding the initial distibution of cells onto the sheet, the definitions above allow us to describe the dynamic evolution of the cells by specifying the procedure for the update of the cell configuration $\boldsymbol{a}^k$ and the hydrogel $\hat{\boldsymbol{q}}^k$ at time $t = k\tau$ to $\boldsymbol{a}^{k+1}$ and $\hat{\boldsymbol{q}}^{k+1}$ at the next time step. We summarize this procedure in Table 1 and Fig. 5.

2.4 Model parameters

Typical dimensions for the cell traction forces are about $10^{-8}\,N$, for the experimental hydrogel geometries $HL = 10^{-8} \dots 10^{-6}\,m^2$ and for the elastic moduli of soft tissues $\mu = 10^3 \dots 10^4$ Pa. We assume that μ does not depend on the concentration and hence we can choose a scaling that eliminates this parameter from the model equations, and also scales the domain to $\hat{\Omega} = [0, 1]^2$. Then we obtain a range of nondimensional traction forces of $f_{\text{trac}} = 10^{-8} N/(\mu HL) = 10^{-6} \dots 10^{-3}$, e.g. cf. [9, 67].

The dynamic model has different time scales: The intrinsic time scale for the ABM motility and orientation dynamics is given by the time step size τ, as cells are updated each time step. However, the practical migration rate then also depends on the magnitude of differences in the deformation function generated by cell-cell and cell-hydrogel interaction. The typical diffusive and solvent in/outflux time scale of the hydrogel then determine the mobilities m and n in (23). We generally assume then that the bulk diffusive mobility is $m = 10^5$. For n, we distinguish two cases. If the solvent is *conserved*, that is, there is not in- or outflux, then of course $n = 0$. Otherwise, in the *non-conserved* case, we assume $n = m$.

Table 2 Model-specific mathematical notation and explanation of symbols

Agent-based model			Hydrogel model		
Symbol	Name	Def	Symbol	Name	Def
$\hat{x}$	Cell position	Sect. 2.3	φ	Volume fraction	Sect. 2.1
d	Cell orientation	Sect. 2.3	$\boldsymbol{c}$	Concentration	Sect. 2.1
n_{cells}	Number of cells	Sect. 2.3	$\boldsymbol{\chi}$	Deformation	Sect. 2.1
A	Single-cell state	Sect. 2.3	$\boldsymbol{F}$	Deformation gradient	Sect. 2.1
$\boldsymbol{A}$	Multi-cell state	Sect. 2.3	J	Jacobian determinant	Sect. 2.1
Ω_{cell}	Cell position set	Eq. (27a)	P	First Piola–Kirchhoff stress	Eq. (8a)
Δ	Cell orientation set	Eq. (27b)	$\boldsymbol{q}$	state vector	Eq. (1)
def	Deformation function	Eq. (29)	$\boldsymbol{\chi}_\Gamma$	Dirichlet boundary cond	Eq. (30)
$\hat{f}$	Traction force	Eq. (28)	$\boldsymbol{x}$	coordinates $(\hat{x}, z) \in \mathbb{R}^3$	Sect. 2.1
δ_x	Dirac δ-distribution		$\hat{x}$	coordinates $(x, y) \in \mathbb{R}^2$	Sect. 2.2
f_{trac}	Traction strength	Eq. (28)	$\mathscr{F}$	Free energy functional	Eq. (1)
$a_i \sim a_j$	Neighboring cells	Table 1	$\mathscr{L}$	Lagrangian functional	Eq. (3)
N	Cell grid size	Eq. (27a)	W	Energy density	Sect. 2.1
N_{dipole}	Dipole count	Eq. (34)	$I(\boldsymbol{c})$	Incompressibility constraint	Eq. (2)

For the evolution in the conserved case, this implies that after each time step with $\tau = 10^{-3}$ the solvent concentration is practically in equilibrium with constant chemical potential η and the total solvent remains equal to its initial value

$$\int_{\hat{\Omega}} (\hat{c} - \bar{c}) \, \mathrm{d}\hat{x} = 0$$

for the given applied strain. The viscoelastic relaxation time is assumed to be smaller than the time step size and thus the evolution is dominated by the ABM's cell dynamics.

For the evolution in the non-conserved case, this equilibrium assumption implies that at each time t the chemical potential is close to zero and the free energy is minimal under the given applied strain, including the possibility of solvent exchange with the surrounding.

For the Gent model we use a moderate limiting deformation $J_m = 2$, consistent with values for biological materials discussed in Sect. 2.1. The prefactor γ in the chemical energy is chosen to be $\gamma = 5 \cdot 10^{-4}$, small enough to regularize the diffusion in regions of large stress differences, e.g. near corner singularities of the elastic sheet. We use representative values for the molecular volume $\alpha = 4$ and choose the initial solvent concentration to be homogeneous $\bar{c} = 0.2$. We assume that the hydrogel energies and equal $k_1 = k_2 = k$ and systematically study the impact of varying k. As we mentioned before, in order to ensure that initially the hydrogel is in equilibrium, we need to set $k_0 = k \ln(\alpha \bar{c})$, where by definition $0 < \alpha \bar{c} < 1$.

Finally, we note that *pure elastic materials* are treated in our hydrogel model as a special case by setting $m = 0 = n$.

For this coupled model no systematic convergence analysis was not performed, as for Dirac-delta forces solutions converge suboptimally in classical function space norms [68, 69]. For the results presented in Sect. 4.3 we combine regularized approximations of Dirac-delta distributions in combination with local mesh refinement, where classical convergence results upon spatial refinement can be expected for fixed regularization.

The model presented in Sect. 2 is applicable in any dimension. However, we focus our discussion here on thin sheets, resulting in two-dimensional problems that are relatively straightforward to solve. Implementing a fully coupled three-dimensional hydrogel model integrated with an agent-based model would be feasible but numerically more time-intensive. While our current focus is on enhancing the fidelity of the ABM, developing a fully three-dimensional model remains a future objective. Some mathematical notation of the hydrogel model and the agent-based model us summarized and a reference to the first definition is given in Table 2.

3 Strain-stiffening effects of hydrogel layers under external load

Before studying interactions with cells in Sect. 4, it is necessary to understand the mechanical response of loaded hydrogel layers under plane strain and plane stress conditions and to carry out comparisons for Gent type and neo-Hooke type elastics networks as well as under conserved and non-conserved conditions. We also compare our results to corresponding problems for pure elastic materials, which have been extensively investigated in the past, e.g. in [70], and are limiting cases of our model.

The geometry of the hydrogel in 2D is fixed as described in Fig. 2 with $L = 1$ so that $\hat{\Omega} = [0, 1]^2$. In order to mea-

sure the mechanical response of the hydrogel we impose an inhomogeneous Dirichlet boundary condition (i.e. an external tensile load) for the deformation

$$\hat{\chi}_\Gamma(t,\hat{x}) = \hat{x} + \begin{cases} 0 & \hat{x} \in \hat{\Gamma}_{\text{bot}} \\ \big(0, \varepsilon_{\text{eng}}(t)\big) & \hat{x} \in \hat{\Gamma}_{\text{top}} \end{cases} \tag{30}$$

with engineering strain $\varepsilon_{\text{eng}}(t) = \varepsilon_{\max} \min(t, 1)$. In other words, the length of the layer is increasingly stretched by an amount $\Delta L = \varepsilon_{\text{eng}}(t) L$ for $0 \le t \le 1$ and then kept fixed at a constant strain $\varepsilon_{\text{eng}} = \varepsilon_{\max}$ for $t > 1$.

In the following, we discuss the ingredients to compute the mechanical stress for an effective 2D hydrogel layer for any given applied (engineering) strain ε_{eng}. For the three-dimensional hyperelastic material with energy density $W(\boldsymbol{F}, \boldsymbol{c}, \nabla \boldsymbol{c})$ as in (1), the first Piola-Kirchhoff tensor defined in (8a) receives its main contribution from $\mathsf{P}_{\text{mech}} = \partial_{\boldsymbol{F}} W_{\text{mech}}$, which for the Gent model (14) is

$$\mathsf{P}_{\text{mech}} = \mu \left(\frac{J_m}{J_m - \operatorname{tr}(\mathbb{C} - \mathbb{I})} \boldsymbol{F} - \boldsymbol{F}^{-T} \right).$$

Similarly, in the limiting case, the neo-Hookean material has the form

$$\mathsf{P}_{\text{mech}} = \mu \boldsymbol{F} \left(\mathbb{I} - \mathbb{C}^{-1} \right) = \mu (\boldsymbol{F} - \boldsymbol{F}^{-T}).$$

At each point these are 3×3 tensors (matrices). The corresponding mechanical contribution to the (symmetric) Cauchy stress is given by $\boldsymbol{\sigma}_{\text{mech}} = J^{-1} \mathsf{P}_{\text{mech}} \boldsymbol{F}^T$. Due to the Lagrange multiplier, we can replace J in W_{chem} by $I(c) = 1 + \alpha(c - \bar{c})$, so that W_{chem} does not directly contribute to the mechanical stresses but only indirectly via the Lagrange multiplier that enforces the incompressibility, i.e. $\mathsf{P} = \mathsf{P}_{\text{mech}} + p J \boldsymbol{F}^{-T}$.

In the two-dimensional approximations we replace the energy density by $W(\boldsymbol{F}_j(\hat{\boldsymbol{F}}, \hat{c}), \hat{c}, \hat{\nabla} \hat{c})$, which induces some minor modifications in the effective stress tensor $\hat{\mathsf{P}}$. In the plane stress approximation we use the chain rule to obtain

$$\hat{\mathsf{P}}_{\text{stress}} = \frac{\partial W}{\partial \hat{\boldsymbol{F}}} = \mathsf{P}_{\text{mech}} \cdot \frac{\partial \boldsymbol{F}_{\text{stress}}}{\partial \hat{\boldsymbol{F}}}, \tag{31}$$

whereas in the plane strain approximation

$$\hat{\mathsf{P}}_{\text{strain}} = \frac{\partial W}{\partial \hat{\boldsymbol{F}}} = \mathsf{P}_{\text{mech}} \cdot \frac{\partial \boldsymbol{F}_{\text{strain}}}{\partial \hat{\boldsymbol{F}}} + \hat{p} \hat{J} \hat{\boldsymbol{F}}^{-T}, \tag{32}$$

using the different expressions for $\boldsymbol{F}_j(\hat{\boldsymbol{F}}, \hat{c})$ for $j \in \{\text{strain}, \text{stress}\}$, respectively. Therefore, for the two-dimensional hydrogel layer, the engineering stress σ_{eng} is calculated in terms of the first Piola-Kirchhoff stress tensor $\hat{\mathsf{P}}$ and using the normal vector $\hat{\nu}$ on $\hat{\Gamma}$ with

$$\sigma_{\text{eng}} = \int_{\hat{\Gamma}_{\text{top}}} \hat{\nu} \cdot \hat{\mathsf{P}} \hat{\nu} \, \mathrm{d}s. \tag{33}$$

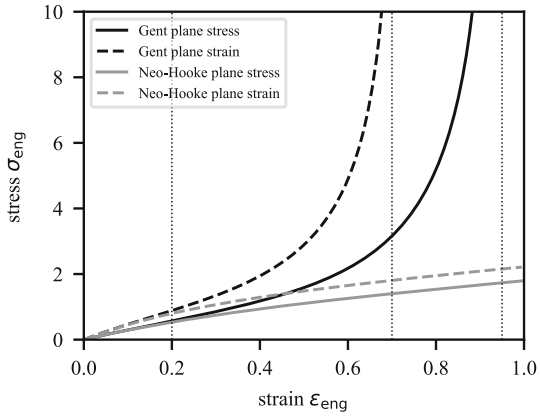

Fig. 6 Stress–strain relation for pure elastic Gent model and pure elastic neo-Hooke model in the plane strain and plane stress approximation. The thin dotted lines show the strains for the plane stress approximation used in Fig. 7

Due to the direct dependence of W_{chem} on J, due to the direct coupling with $I(\boldsymbol{c})$ and due to the indirect coupling with the Lagrange multiplier the engineering stress of the layer depends on all the hydrogel parameters. The same coupling will result in an inhomogeneous solvent concentration c when an external stress is applied.

Layers of pure elastic materials

In Fig. 6, as reference curves we show the stress–strain relation for a pure elastic Gent (black lines) and neo-Hooke model (grey lines) in the plane strain (dashed lines) as well in the plane stress (solid lines) approximation. The plane stress approximation is suitable for systems of thin elastic sheets that expand and shrink in the sheet direction and change thickness without considerable bending or wrinkling. The plane strain approximation is suitable for thick elastic layers, where the deformation is primarily within one plane and negligible in the orthogonal direction.

The strain-stiffening capability of the Gent model for both plane strain and plane stress can be directly observed in the stress–strain relation in Fig. 6, where the stress for the Gent model grows super-linearly (stiffening) and for the neo-Hooke model it grows sub-linearly (softening). For small engineering strains $0 < \varepsilon_{\text{eng}} < 0.2$, Gent and neo-Hookean materials follow the same (linear elastic) behavior with different effective elastic bulk modulus for plane strain (stiffer) and plane stress (softer), respectively. The same behavior can also be observed in Fig. 7, where we show the trace $\operatorname{tr}(\mathbb{C} - \mathbb{I})$ indicating that value of that term in the free energy density of the Gent and neo-Hookean material. For $\varepsilon_{\text{eng}} = 0.2$ both materials show qualitatively the same behavior with large

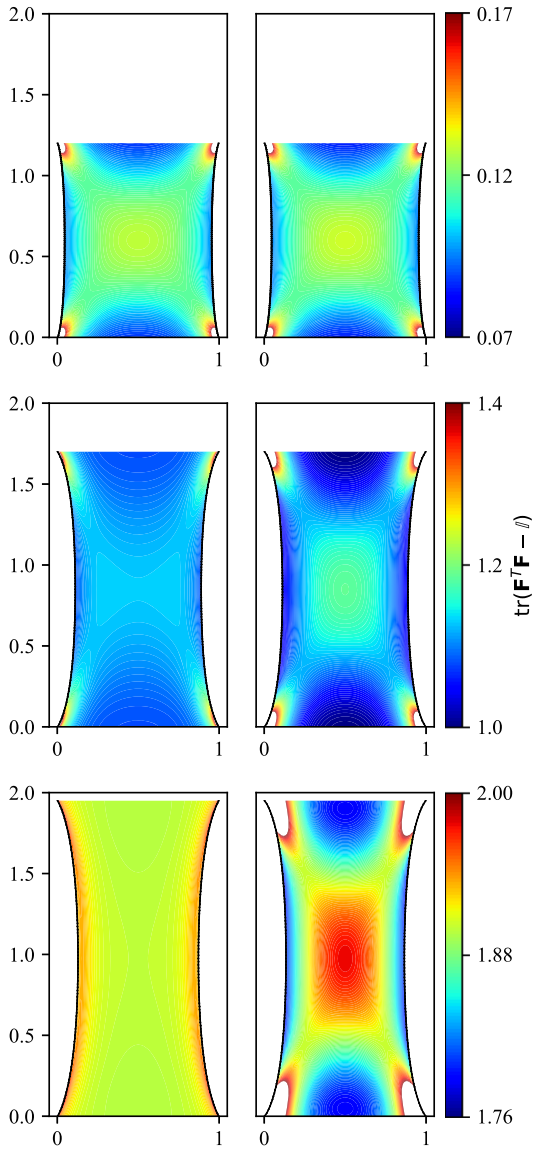

Fig. 7 Stretching of (left column) pure elastic Gent material with $J_m = 2$ and of (right column) neo-Hookean material for increasing engineering strain (top to bottom) of $\varepsilon_{\text{eng}} = 0.2, 0.7, 0.95$. The colored shading in each row shows $\text{tr}(\boldsymbol{F}^T\boldsymbol{F} - \mathbb{I})$ and for the Gent model never exceeds J_m. In each row, the (left) and (right) panel share a color bar, where white areas indicate that values exceed its range

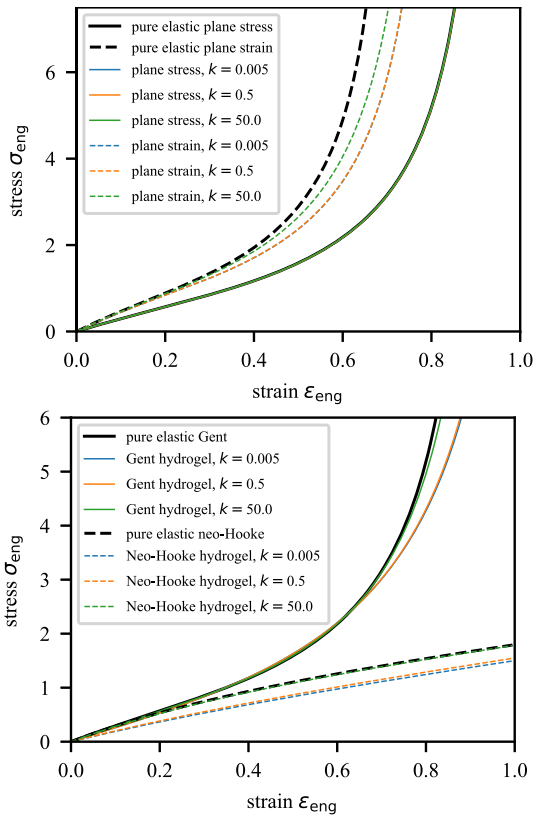

Fig. 8 (top) Stress–strain relations for Gent-type hydrogels for the conserved case under plane stress and plane strain conditions compared to pure elastic behavior. (bottom) Stress–strain curves for the plane stress condition for Gent and neo-Hooke type hydrogels in the non-conserved case compared to the pure elastic material behaviour

deformation gradients in the corner of the elastic sheet. For larger strain $\varepsilon_{\text{eng}} = 0.7$ the strains starts to differ both in the corner and in the center of the sheet, where the neo-Hookean material has systematically larger deformations encoded in $\text{tr}(\mathbb{C} - \mathbb{I})$. Near the stress singularity $\varepsilon_{\text{eng}} = 0.95$, the Gent material stiffens with $\text{tr}(\mathbb{C} - \mathbb{I})$ close to J_m, whereas the softer neo-Hookean material develops even more singular deformation gradients in the corner of the elastic sheet. In general, one may stretch the neo-Hookean sheets much further than sheets of Gent-type, since for the latter $\ln\left(1 - J_m^{-1}\text{tr}(\boldsymbol{F}^T\boldsymbol{F} - \mathbb{I})\right)$ becomes singular for a certain maximal sustainable engineering strain at which the corresponding stress becomes infinite. That maximal engineering strain depends on several parameters, e.g. on the geometry, on the elastic parameters μ and J_m, but also on the hydrogel energy and the type of 2D approximation.

Hydrogel layers

For hydrogels with conserved solvent concentration the stress–strain relationship of thin sheets as described by the plane stress approximation only shows small differences to that of a pure elastic material. This is visible in Fig. 8 (top) where the solid curves for hydrogels for different values of k and the pure elastic material overlap. This behavior is shown for Gent-type materials and is similar for neo-Hookean hydrogels (not shown). However, in the plane strain approximation this changes. In this case the stress–strain curves are dependent on the values of the parameter k in the Flory-Huggins energy, i.e for large values of k the stress–strain relation converges to that of the pure elastic model, whereas for lower k values the engineering stress decreases, see the dashed lines in Fig. 8 (top). Regarding the independence of the stress–strain relation for the plane stress case we note that the mechanical energy is expanded around the refer-

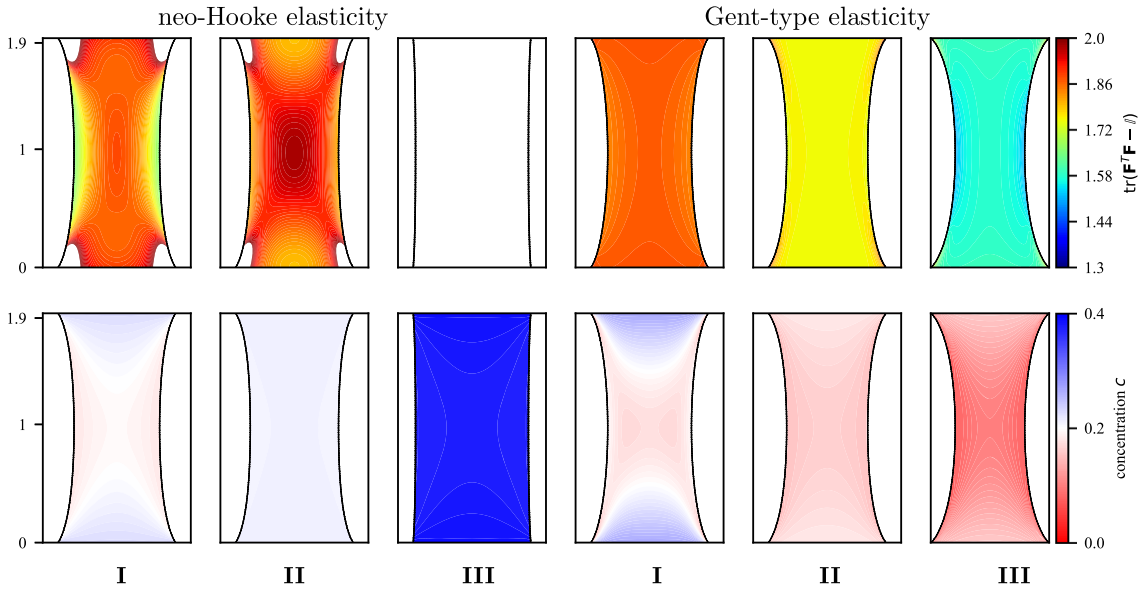

Fig. 9 Comparison of stretched hydrogels in the plane stress approximation at an engineering strain $\varepsilon_{\text{eng}} = 0.94$. In the first row $\text{tr}(\boldsymbol{F}^T\boldsymbol{F} - \mathbb{I})$ is illustrated, while in the second row the solvent concentration c. From left to right we present the results for neo-Hooke elasticity: (column I) neo-Hooke hydrogel for the conserved case and $k = 0.5$, neo-Hooke hydrogel for the non-conserved case and (column II) $k = 50$ and (column III) $k = 0.5$. For the Gent-type elasticity we show (column I) Gent hydrogel for the conserved case and $k = 0.5$, Gent hydrogel for the non-conserved case and (column II) $k = 50$ and (column III) $k = 0.5$

ence state with $\boldsymbol{F} = \mathbb{I}$ and $\hat{c} = \bar{c}$ so that variations are smaller compared to a pure elastic model for a hydrogel expanded around the dry state $\hat{c} = 0$ as the reference. Again, the behavior is qualitatively similar for a neo-Hookean material (not shown).

However, if we allow for a solvent flux into or out of the hydrogel to describe exchange with a surrounding solvent bath, then also in the plane stress limit the stress–strain relation and the stiffness differs significantly from that of a pure elastic material, cf. Figure 8 (bottom). For large k, the material behavior is closer to that of the pure elastic material and for smaller k the material gets softer. This effect should not be confused with drying induced softening or stiffening but is purely related to the change in hydrogel volume that allows a further reduction of the total free energy of the system as opposed to the conserved elastic system, where such a change of volume is impossible. These observations demonstrate the importance of distinguishing between stiffening and softening effects in hydrogels that are caused by strain, solvent drying or even just solvent redistribution by diffusion. The main difference between the stress–strain relation of the neo-Hookean hydrogel and the Gent hydrogel shown in Fig. 8 (bottom) is that while for neo-Hookean hydrogel the deviation from pure elastic behavior is evident for all strains, for Gent-type hydrogels it differs significantly only for large strains.

In the first row of Fig. 9, $\text{tr}(\boldsymbol{F}^T\boldsymbol{F} - \mathbb{I})$ is presented at an engineering strain of $\varepsilon_{\text{eng}} = 0.94$ for the plain stress approximation of the neo-Hooke and Gent hydrogel models with conserved solvent concentration and non-conserved solvent concentration for different k. Furthermore, the corresponding solvent concentrations are highlighted in the second row of Fig. 9.

Interestingly, Fig. 9 reveals significant qualitative differences between neo-Hookean hydrogels and Gent-type hydrogels upon stretching. Firstly, while for large k both hydrogels behave like their elastic counterparts, for sufficiently small k the neo-Hookean hydrogel absorbs solvent upon stretching and therefore, increases its volume, the Gent-type hydrogel releases solvent upon stretching and therefore, reduces its volume. This effect can be most prominently seen in the lower row of Fig. 9, for the neo-Hooke elasticity in column III showing absorption and for the Gent-type elasticity in column II, showing release of solvent. In particular for the neo-Hookean material this results in the strikingly different cross-section shape, where the deformed side boundaries are almost straight due to solvent absorption. With conserved solvent concentration, the lower panels for neo-Hooke column I and Gent column I show that solvent diffusion due to stretching leads to lower solvent concentration in the middle area of the sheet and higher solvent concentration near the top and bottom boundaries. Additionally, in the upper panel for Gent column I we observe the strain-stiffening effect already seen in Fig. 7 for the pure elastic material. In particular in the upper panels for the Gent model (columns II and III) one can see that with lower k the hydrogel mechan-

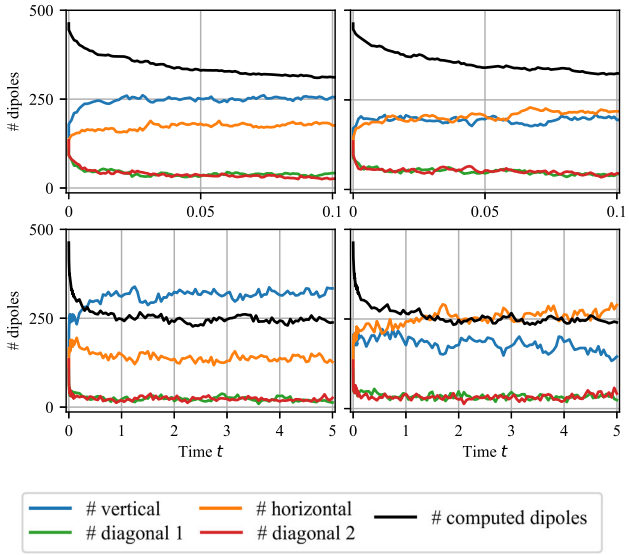

Fig. 10 Number of cells with different orientation and effective dipole count for the pure elastic neo-Hookean material without external load (left) under plane stress condition and (right) under plane strain condition, where the number of computed dipoles are calculated using (34)

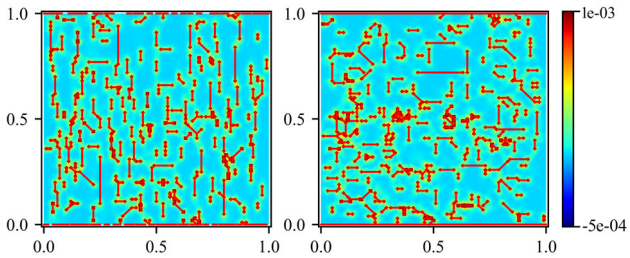

Fig. 11 Final cell configuration without load after $T = 5$, i.e. 5000 iterations. Pure elastic neo-Hookean material (left) under plane stress condition and (right) under plane strain condition. The colored surface represents strain $\mathrm{tr}(\boldsymbol{F}^T\boldsymbol{F} - \mathbb{I})$ and the red lines the cells

ical energy is reduced and therefore, the material becomes softer.

The consistent coupling of such effects in biological hydrogels is a necessity for a fundamental understanding of such a complex system in order to make meaningful predictions that are able to distinguish from more complex biological processes, where cell movement depends on biochemical signaling processes in addition to mechanical stimuli, which can be modeled with such a system.

4 Collective migration of cells on hydrogel layers

The main focus of this section is the discussion of interactions between cells and hydrogels, i.e. with Gent-type or neo-Hookean elastic models under the plane strain or plane stress condition for conserved or non-conserved solvent. For comparison, we will also investigate the interaction of cells with pure elastic materials under the plane strain and plane stress condition.

We first investigate the effects on cell migration and pattern formation for $\varepsilon_{\mathrm{eng}} = 0$ in Sect. 4.1. Note that due to the different boundary conditions at the top/bottom and the side boundaries, cells can have a preferred orientation even without any stretching of the layer. This orientation may change once we apply, in Sect. 4.2, a non-zero engineering strain $\varepsilon_{\mathrm{eng}}$ to stretch the layer. We generated a random distribution of 500 cells and use it as initial distribution for all numerical studies for better comparison of the pattern formation. For the traction force for a single cell we set $f_{\mathrm{trac}} = 10^{-3}$ as motivated in the previous section. In Sec. 4.3 we provide a qualitative analysis of the phenomena observed by detailed local case studies of the deformation function used by the ABM.

The evolution of cell patterns and orientations entails the corresponding evolution of the number of horizontal, vertical and diagonal cells. Notably, cells have a tendency to aggregate, mostly into chains. We thus define an approximation of the number of dipoles, and the number of chains, via

$$N_{\mathrm{dipole}} = \frac{1}{2 f_{\mathrm{trac}}} \int_{\hat{\Omega}} |\hat{f}_x(t,\hat{x})| + |\hat{f}_y(t,\hat{x})| \, \mathrm{d}\hat{x}, \tag{34}$$

where $\hat{f}_x$ and $\hat{f}_y$ are the x and y components of $\hat{f}$ as given in (28). For a straight horizontal or vertical chain, the δ-functions making up the cell dipoles cancel out, except for the first and the last one in the chain. Hence each such a chain contributes a count of 1 to N_{dipole}. The same is true for an isolated cell, which is therefore treated as a chain which contains one cell only. If the chain is not straight or forks, the contribution is slightly different, but these aggregates are rare. Hence, to a good approximation, N_{dipole} counts the number of chains in a cell distribution.

4.1 Cells without external load

We first investigate the cell interaction with material layers without an external load, starting with pure elastic material models. In this case, deformations are induced solely by the cells and are small so that we essentially remain in the linear regime, where the neo-Hooke and the Gent models agree. Therefore, for the pure elastic case we will discuss our results only for the neo-Hooke model.

We begin with a comparison of the number of vertical, horizontal and diagonal dipoles. Figure 10 shows that the number of diagonal dipoles (green and red) decreases rapidly for the plane stress and plane strain cases and the cells are mainly horizontally (orange) and vertically (blue) orientated. In the plane stress case shown in Fig. 10 (left) the cells favor a vertical orientation, while in the

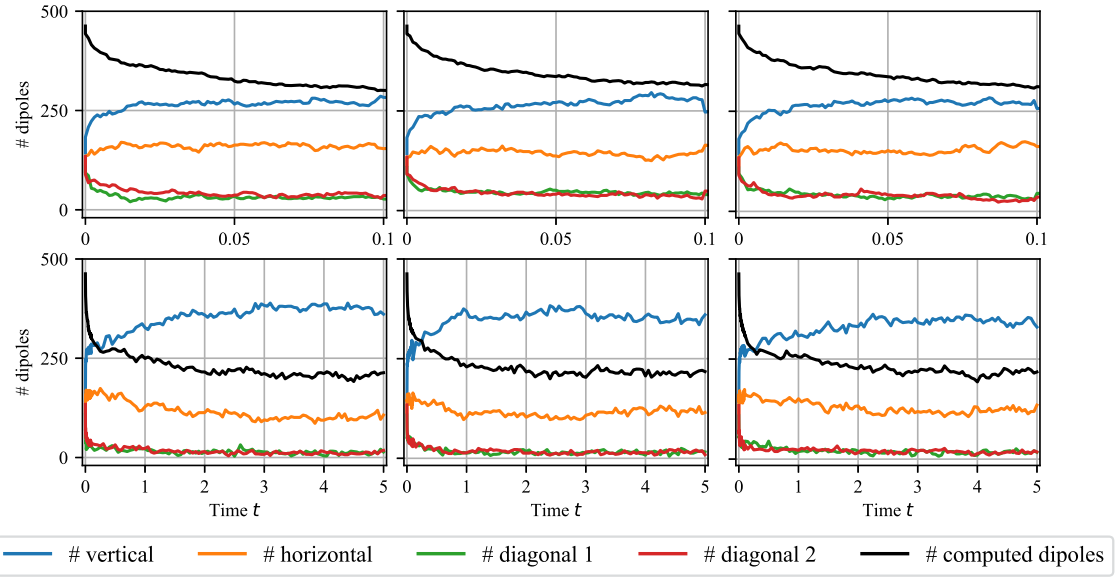

Fig. 12 Number of cells with horizontal, vertical or diagonal orientation and effective number of computed dipoles for the non-conserved neo-Hooke hydrogel with (left), for the non-conserved Gent hydrogel with (middle), and for the conserved Gent hydrogel (right) under plane stress condition. In all cases we set $k = 0.5$

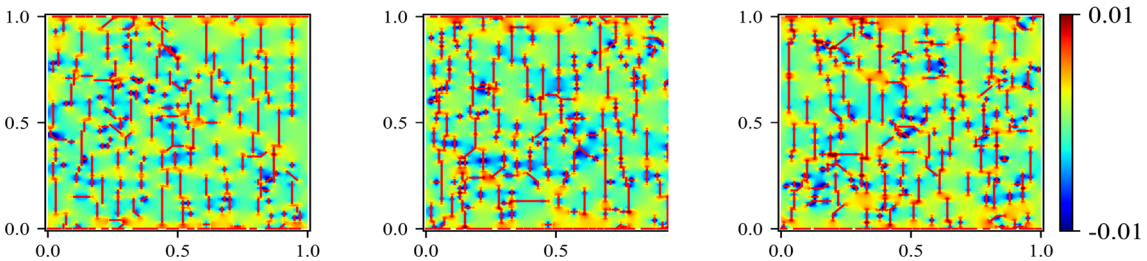

Fig. 13 Cell configuration without stretching at $T = 5$, i.e. after 5000 iterations. As in Fig. 12 we show the non-conserved neo-Hooke hydrogel (left), non-conserved Gent hydrogel (middle), and the conserved Gent (right) under plane stress condition. In all cases we set $k = 0.5$. The colored surface represents strain $\mathrm{tr}(\boldsymbol{F}^T\boldsymbol{F} - \mathbb{I})$ and the red lines the cells

plane strain case (right) horizontal orientations are favored. Moreover, the difference between the vertical and horizontal orientation is less pronounced in the plane strain case. Interestingly, in both situations the number of computed dipoles is comparable. This indicates that the cells form long-range alignments in both cases. We note that the effect in the plane stress situation has been observed before in [9].

Considering the long-time cell patterns Fig. 11 illustrates that while for the plane stress case dipole orientations are predominantly vertical, in the plane strain case the small difference in the number of vertical and horizontal dipoles is apparent and seems to be associated with the formation of clusters. Also note, in both cases almost the complete fixed boundaries are covered by cells. Moreover, if the cells on the clamped boundary are ignored, the difference between vertical and horizontal dipoles would increase in the case of plane stress, while in the case of plane strain, the number of vertical and horizontal dipoles would become much closer.

A comparison of the corresponding hydrogels under plane strain and plane stress condition shows similar results and we focus here on hydrogels under plane stress. We compare the non-conserved neo-Hooke hydrogel case, the non-conserved Gent-type hydrogel and the conserved Gent-type hydrogel, all for $k = 0.5$, in Figs. 12 and 13. The results are similar to the plane stress case of the pure elastic material in Figs. 10 and 11.

4.2 Cells on stretched sheets

We now investigate the cells' response to applying a finite strain via stretching the hydrogel layers in our numerical experiments. All other parameters and initial settings are cho-

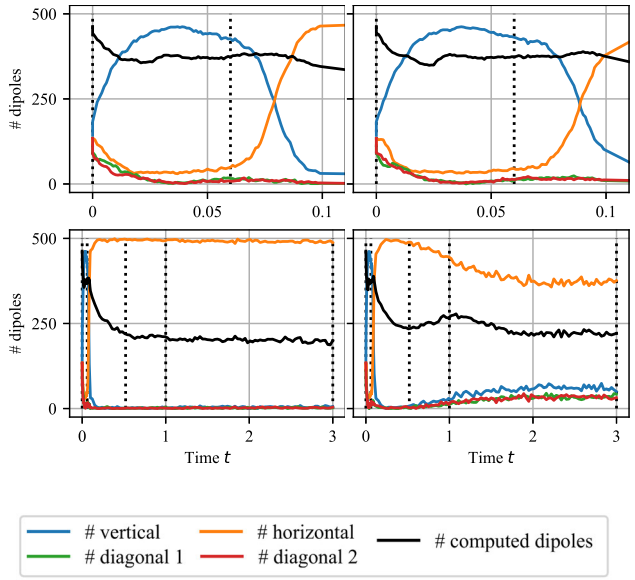

Fig. 14 Number of cells with horizontal, vertical or diagonal orientation and effective number of computed dipoles in a stretched hydrogel with $\varepsilon_{\text{eng}} = \varepsilon_{\max} \min(t, 1)$ with $\varepsilon_{\max} = 0.9$ computed (left) for the neo-Hookean hydrogel and (right) for the Gent-type hydrogel. In the (lower panel) the history $0 \leq t \leq 3$ and the the (upper panel) the initial stage for $0 \leq t \leq 0.1$ is shown. The dotted lines indicate the time of the snapshots shown in Figs. 15 and 16, i.e. $\varepsilon_{\text{eng}} = \{0, 0.06, 0.51, 0.9, 0.9\}$ from left to right

sen as in the previous subsection. In this section we consider the evolution of hydrogels with non-conserved solvent concentration for neo-Hooke and Gent-type materials only in the plane-stress limit, that is for thin sheets.

Similarly to the experimental procedure of stretching hydrogel layers in Sect. 3 we ramp up the engineering strain $\varepsilon(t) = \min(1, t)\varepsilon_{\max}$.

In the upper left and right panel of Fig. 14 we observe that for early times $0 < t < 0.1$ the neo-Hookean and Gent-type hydrogel evolve in the same way, since they have the same linear material behavior. Remarkably, between $t = 0.05$ and $t = 0.1$ we observe a change from mainly vertically to mainly horizontally orientated cells. Usually, the response of cell orientation to a change of local elastic behavior is relatively fast compared to migration and chain formation. Diagonal orientation of cells is negligible for both neo-Hookean and Gent-type materials for most of the time. This bias is caused by the larger distance of the centers of the δ-functions in (28) for diagonal orientations, thus driving the cells to align horizontally or vertically with the mesh. Only strong diagonal strains imposed by the surrounding cells or through external loading of the sheet will lead to diagonal cell orientations.

In the lower panels of Fig. 14 the neo-Hookean horizontal orientation for $1 < t < 3$ stays basically constant, while for the Gent-type hydrogel the number of horizontal cells reduces at the expense of vertical and diagonal cells that accumulate at the top and bottom boundary. Considering the effective dipole number, cell chains continue to grow in length for the neo-Hookean material, while for the Gent-type material, the rapid change in cell configuration during the interval of $0.5 < t < 1$ leads to a reduction in chain length.

Figure 15 shows the typical strain and solvent concentration and the corresponding cell patterns during the initial stretching $0 \leq t \leq 1$ of a neo-Hookean hydrogel (a–d) and for later times (e) $t = 3$. It can be seen that the initially random cell configuration from panel (a) at $t = 0$ leads to a vertical orientation of the cells after a short time, as can be seen in (b). Beyond a strain of $\varepsilon_{\text{eng}} = 0.1$, the cells orient themselves horizontally (c) and after some time form longer chains (d). As the chain formation progresses further, on a longer time scale cells accumulate at the lower and upper boundary of the thin hydrogel sheet, (e) at $t = 3$. However, since the neo-Hookean hydrogel does not contract as much due to solvent desorption as previously observed in Fig. 9 column III, a significant proportion of the cells remain in the inner area of the sheet.

From the point of view of the loading and hydrogel parameters, the stretching experiment with the Gent-type model in Fig. 16a–c is performed analogously. However, as already shown in Fig. 9, the solvent leaves the Gent-type hydrogel and thus reduces the total volume. While the same transition from vertical to horizontal cell orientation can be observed as for the neo-Hookean material, especially at the beginning of the tensile experiment, the much stronger constriction of the hydrogel leads to a stronger migration of the cells and thus to a rapid accumulation at the lower and upper edge of the thin sheet visible in (d) and (e).

4.3 Detailed study of one- and two-cell configurations

We now show how the main features of migrating cell populations on hydrogels as observed in Sects. 4.2 and 4.1, can be understood by an analysis of the hydrogel-cell system for one- and two-cell configurations $\boldsymbol{a} \in \boldsymbol{A}$.

Both migration and orientation are governed by the ABM via the deformation function $\text{def}(\hat{\boldsymbol{q}}, \boldsymbol{a}) \geq 0$ from (29). Due to the update proposed for the ABM in Table 1, cells $\boldsymbol{a} = (\hat{x}, d)$ favor positions $\hat{x}$ and orientations d for which the deformation function is minimal.

One-cell configurations.

For a given time-independent single cell state $\boldsymbol{a} = (\hat{x}, d) = \boldsymbol{a}_1 \in \boldsymbol{A}$ with $n_{\text{cells}} = 1$ we compute the traction force $\hat{f}(\boldsymbol{a}_1)$ and solve the corresponding (stationary) hydrogel problem for $\hat{\boldsymbol{q}}_1(\boldsymbol{a}) = \lim_{t\to\infty}(\hat{\boldsymbol{q}}(t))$. With this solution

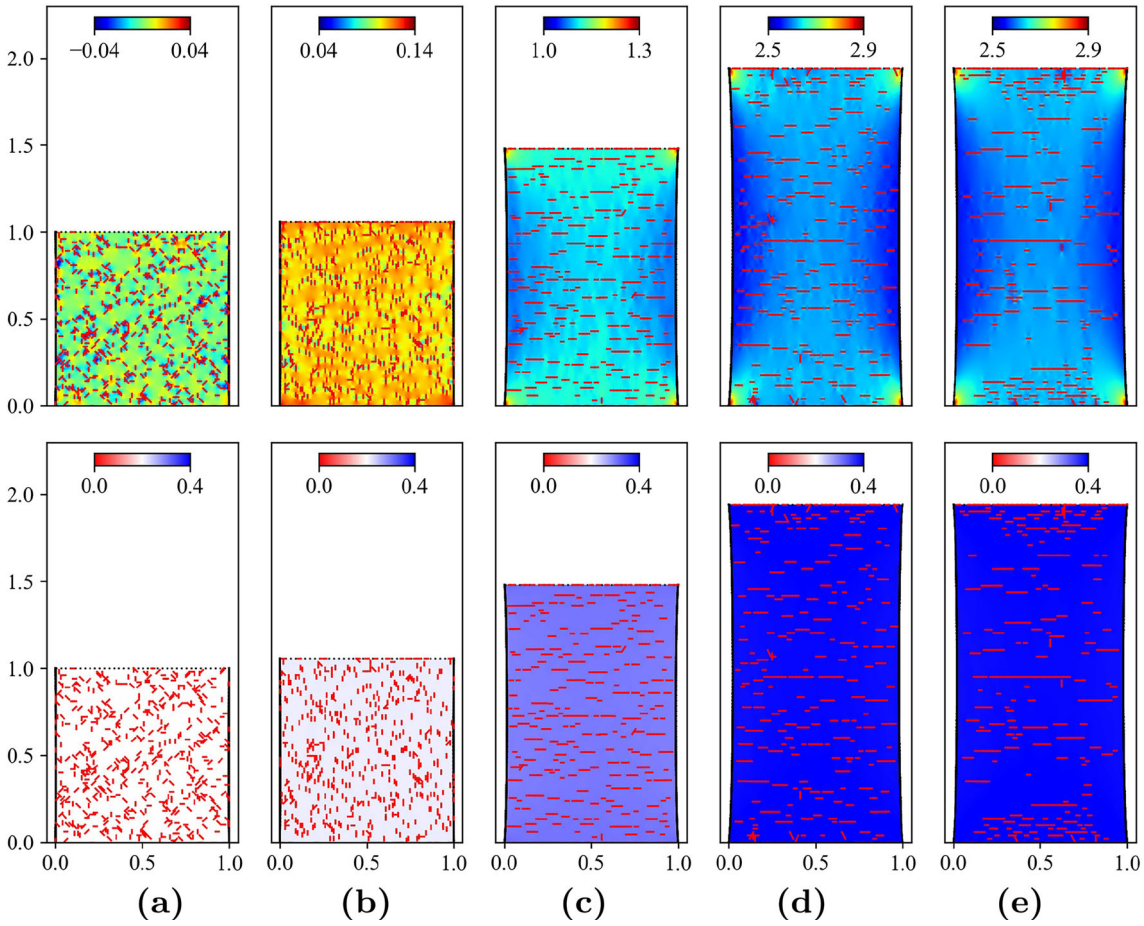

Fig. 15 Neo-Hookean hydrogel with $k = 0.5$ and non-conserved solvent concentration for increasing strain $0 \leq \varepsilon_{\text{eng}} \leq 0.95$ from left to right showing **(a)** initial configuration, **(b)** $\varepsilon_{\text{eng}} = 0.06$, **(c)** $\varepsilon_{\text{eng}} = 0.51$ and **(d, e)** $\varepsilon_{\text{eng}} = 0.9$. The (upper panel) shows strains $\text{tr}(\boldsymbol{F}^T\boldsymbol{F} - \mathbb{I})$ (Note: color bar changes) and the (lower panel) shows concentrations $\hat{c}$

we evaluate the one-cell deformation

$$\text{def}_1(\boldsymbol{a}) := \text{def}(\hat{\boldsymbol{q}}_1(\boldsymbol{a}), \boldsymbol{a}), \tag{35}$$

in order to determine, for example, the most likely orientation. Therefore, for fixed cell position $\hat{x}$ one needs to find the orientation $d \in \Delta$ for which $\text{def}_1((\hat{x}, d))$ is smallest. Similarly, by plotting the function $\text{def}_{1,\hat{x}}(\hat{x}) = \min_{d\in\Delta} \text{def}_1(\hat{x}, d)$ one finds the places where the deformation function has a local or global minimum and therefore are places that cells would migrate to by cell-hydrogel interaction.

In Fig. 17a and d the corresponding comparison of the neo-Hookean elastic material in the plane strain and in the plane stress approximation, respectively, is shown without external load, i.e. $\varepsilon_{\text{eng}} = 0$. While in the plane stress approximation vertical orientation is favored at all points, in the plane strain approximation the central region also supports horizontally oriented cells. If the full ABM is applied to iterate also over position, the single cell will favor locations close to the top and bottom boundary due to the smaller deformation, where they would be constrained to the horizontal orientation, as observed in Fig. 11 for multi-cellular distributions.

We also quantify the cell's preference regarding orientation and position on stretched neo-Hookean layers in the remaining panels of Fig. 17. Here we clearly observe that for small strains $\varepsilon_{\text{eng}} < 0.1$ (plane strain) and $\varepsilon < 0.05$ (plane stress) the preference for vertical orientation persists, but that the trend is reversed for larger strains (here shown for the plane stress). We also note that close to the transition, the local deformation function changes qualitatively, as shown for the plane-stress case. This explains how the strain-induced transtion from a vertical to a horizontal orientation observed for the multi-cell configurations is directly encoded in the ABM via the current choice of the deformation function.

In Fig. 18 we extend the single-cell analysis to strongly stretched neo-Hookean hydrogels (right) compared to pure

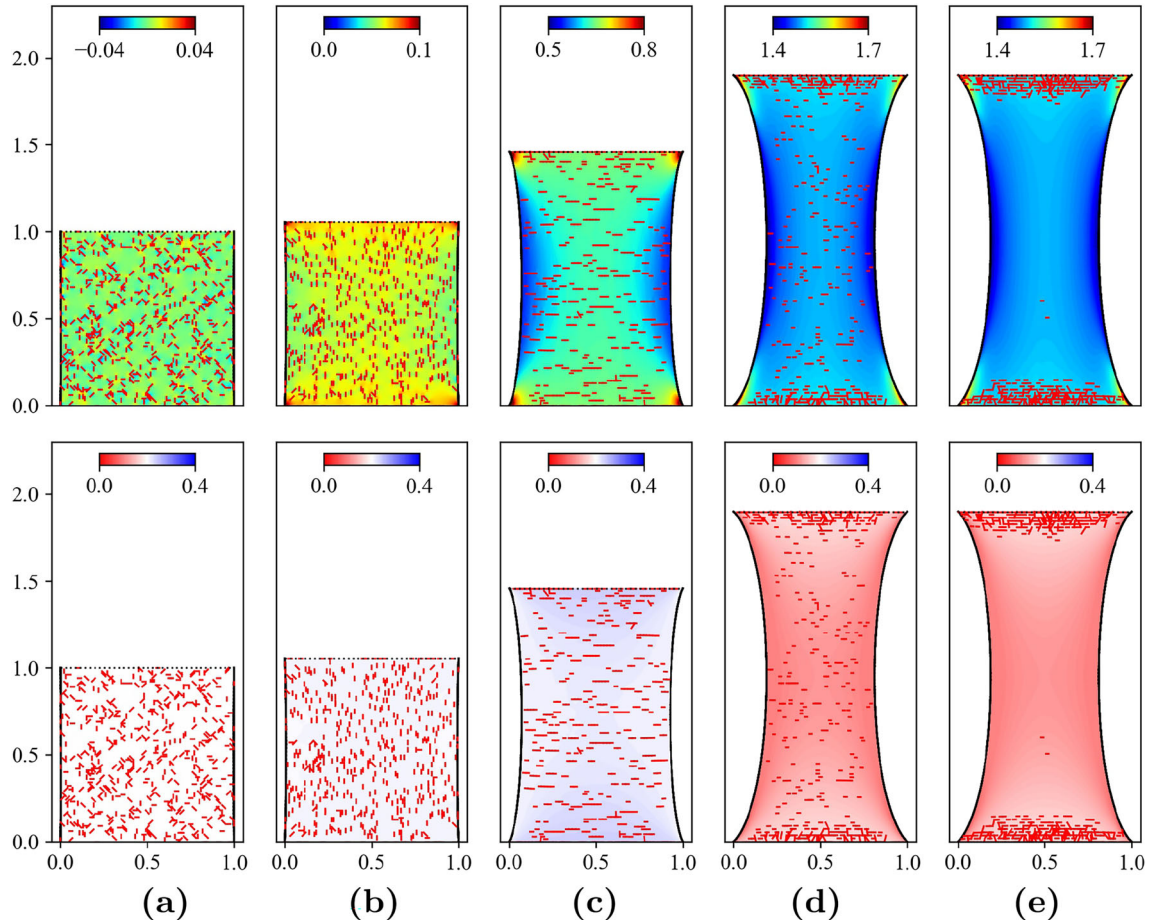

Fig. 16 Gent-type hydrogel with $k = 0.5$ with non-conserved solvent concentration and increasing strain $0 \leq \varepsilon_{\text{eng}} \leq 0.95$ from left to right for **(a)** initial configuration, **(b)** $\varepsilon_{\text{eng}} = 0.06$, **(c)** $\varepsilon_{\text{eng}} = 0.51$ and **(d, e)** $\varepsilon_{\text{eng}} = 0.9$. The (upper panel) shows strains $\text{tr}(\boldsymbol{F}^T\boldsymbol{F} - \mathbb{I})$ and the (lower panel) shows concentrations $\hat{c}$

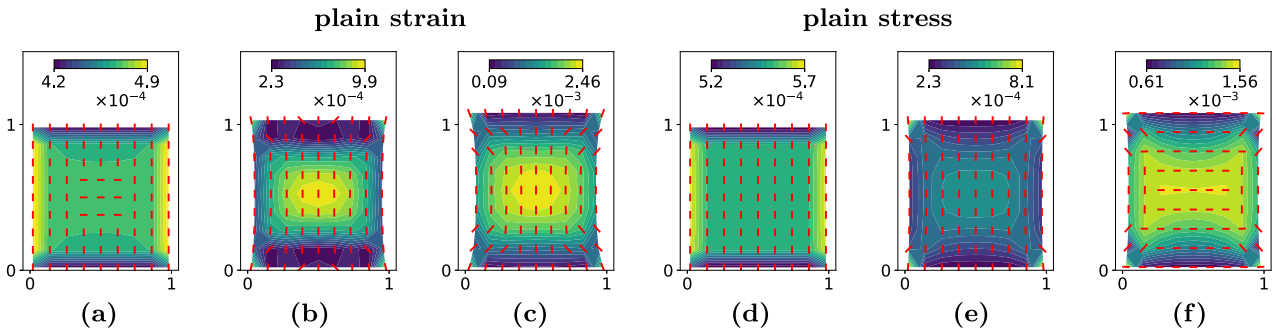

Fig. 17 Single cell deformation $\text{def}_1(\boldsymbol{a})$ on neo-Hookean elastic layers with no or small external load for the plane strain **(a–c)** and plain stress **(d–f)** approximation. The engineering strain in **(a, d)** is $\varepsilon_{\text{eng}} = 0$, in **(b, e)** it is $\varepsilon_{\text{eng}} = 0.05$ and in **(c, f)** we use $\varepsilon_{\text{eng}} = 0.1$

elastic materials (left). While both show a clear preference for a horizontal cell orientation, the variations in the single-cell deformation function are much smaller leading to a somewhat smaller migration rate.

Two-cell configurations.

Similarly, the cell-cell interaction can be studied using two time-independent cells $\boldsymbol{a}_2 = (\boldsymbol{a}, \boldsymbol{a}^*) \in \boldsymbol{A}$ with $n_{\text{cells}} = 2$. Here, we fix one cell at the center of the domain with a fixed orientation, i.e. $\boldsymbol{a}^* = (\hat{x}^*, d^*)$ with $\hat{x}^* = (L/2, L/2) \in \Omega_{\text{cell}}$ and $d^* = d_{\updownarrow}$. Then we set $Va = (\hat{x}, d) \in A$ arbitrary, compute the traction force $\hat{f}(\boldsymbol{a}_2)$ and solve the corresponding (stationary) hydrogel problem for $\hat{\boldsymbol{q}}_2(\boldsymbol{a}) = \lim_{t\to\infty}(\hat{\boldsymbol{q}}(t))$. Based on this solution, we define the two 2-cell deformations

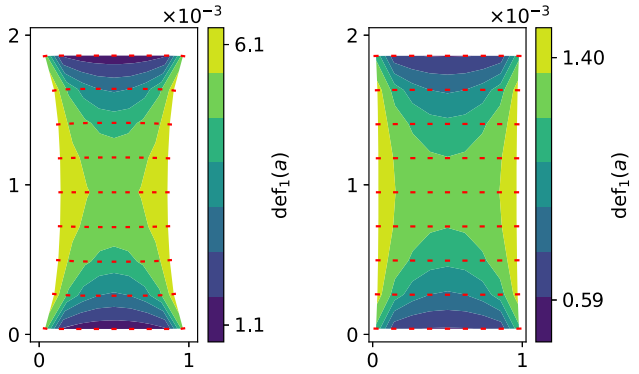

Fig. 18 Cell-hydrogel interaction for strongly stretched elastic sheet from single cell computation showing $\mathrm{def}_1(\boldsymbol{a})$ for neo-Hookean material in the plane stress approximation. We show (left) the pure elastic material and (right) the non-conserved solvent with $k = 0.5$

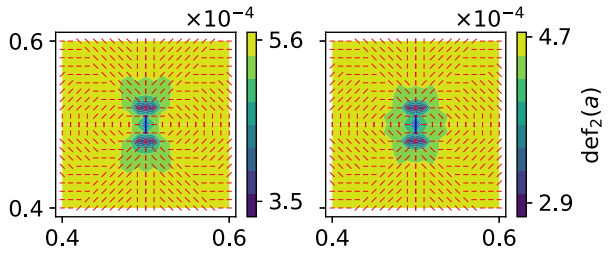

(a) plane stress neo-Hooke (b) plane strain neo-Hooke

Fig. 19 Cell-cell interaction from double cell computation showing $\mathrm{def}_2(\boldsymbol{a})$. The red line indicates the optimal cell orientation of a second cell and the colors shows the optimal cell location based on the smallest value of the deformation function. The first cell is fixed at $\hat{x} = (0.5, 0.5)$ with a vertical orientation (blue line)

$$\mathrm{def}_2(\boldsymbol{a}) := \mathrm{def}(\hat{\boldsymbol{q}}_2(\boldsymbol{a}), \boldsymbol{a}), \tag{36}$$

$$\mathrm{def}_2^*(\boldsymbol{a}) := \mathrm{def}(\hat{\boldsymbol{q}}_2(\boldsymbol{a}), \boldsymbol{a}^*), \tag{37}$$

relative to the given cell $\boldsymbol{a}^*$, where up-to discretization artifacts due to the singular nature of the traction force $\hat{f}$, both definitions should give rise to the same interpretation of cell-cell interactions. As before, from $\boldsymbol{a}$ we can deduce most likely orientations and cell positions.

In Fig. 19 we show the resulting two-cell deformation function based on def_2^* and observe that cell-cells interactions favor formation of chains with cells $\boldsymbol{a}$, $\boldsymbol{a}^*$ of same orientations being at positions $\hat{x}^* = \hat{x} \pm 2d$. However, note that the magnitude of cell-cell interaction is $\sim 10^{-4}$, whereas the cell-hydrogel interaction is usually stronger with $\sim 10^{-3}$ and therefore dominates the cell dynamics. Also, cell-hydrogel interaction is usually a long-range effect whereas cell-cell interaction is extremely short-ranged and limited to a few diameters of cell-dipole distances. The cell-cell interaction map shown in Fig. 19 confirms the previously made observation that cells tend to form chains, although in a transient regime this effect may be disrupted by external strain fields as we observed in the right panel of Fig. 14. This investigation of the deformation function shows that single and double-cell investigations provide a basic understanding of the collective pattern formation and the migration and (re)orientation of cells in external strain fields.

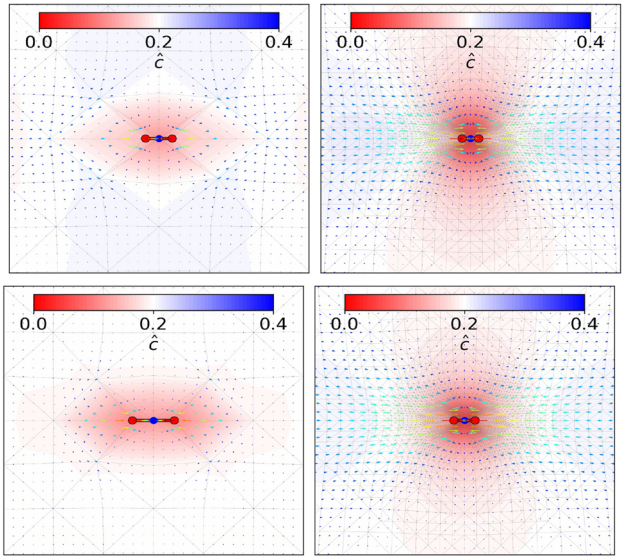

Fig. 20 Concentration and deformation in the region $[0.47, 0.53]^2 \subset \hat{\Omega}$ of a single horizontal cell at $\hat{x} = (0.5, 0.5)$ on spatially uniformly and (locally) highly resolved computational meshes. (Upper left) neo-Hookean uniform vs (upper right) neo-Hookean highly resolved and (lower left) Gent uniform vs (lower right) Gent highly resolved with large traction force $f_{\mathrm{trac}} = 4 \cdot 10^{-2}$. The shading shows the concentration with red, white and blue corresponding to $c \approx 0$, $c \approx \bar{c} = 0.2$ and $c \approx 0.4$. The colored vector field shows the displacement field and the thin gray mesh displays the deformed computational mesh

Effects of single cells on strain-stiffening hydrogels, have been observed for example in [71] or in [72, 73]. Within our current hydrogel-ABM model framework the tensorial computational meshes, such that the vertices of the triangle mesh for the finite element approximation $\hat{\Omega}$ coincide with the cell positions Ω_{cell}. However, since a cell at $\hat{x}$ exerts a dipole-like force a neighboring mesh vertices $\hat{x} \pm d$, in particular the near-field of the hydrogel deformation and concentration could be underresolved. To illustrate the impact, we compare in Fig. 20 deformation and concentration profile near a single cell at $\hat{x} = (0.5, 0.5)$ for underresolved (left panels) and highly resolved (right panels) hydrogels for neo-Hookean (upper panels) and Gent (lower panels) hydrogels. Here, instead a dipole generated by Dirac measures we approximate $\delta_{\hat{x}} \approx (2\pi\varepsilon)^{-1} \exp(-\frac{1}{2\varepsilon}|x - \hat{x}|^2)$ with $\varepsilon = 10^{-6}$ and successively increase the traction force to its maximal value to find a stationary solution of the nonlinear hydrogel problem. This shows a good approximation of the elastic problem on a coarse grid, since for the ABM in its current form, only

the deformation in the vicinity of the cell is of importance. However, in particular the effect of solvent displacement due to cell traction on the coarse grid is underestimated. In order to investigate possible qualitative different behavior of the cell population for the Gent-type and neo-Hookean hydrogels in the regime, where strain-stiffening effects become relevant, it will be necessary to allow for a higher spatial resolution near cells. This will also allow to robustly generate larger traction forces in the strain-stiffening range and thus cells become active agents and establishes mechanical reciprocity of the cell-hydrogel interactions. This will further entail modifications of the ABM that also account for hydrogel stiffness for example via a second derivative of the mechanical energy, for example as introduced in [67, 74, 75], or the viscosity [76].

5 Conclusion and outlook

We used hydrogels as a bottom-up approach for designing three-dimensional models that mimic certain properties of a native ECM environment, e.g. swelling and solvent diffusion. For this we have developed a model framework that couples a continuum two-component system for a viscoelastic hydrogel with an agent-based model that governs the migration decisions of each cell as it interacts with the hydrogel and other cells of the population. This model framework for the cell-hydrogel system can be systematically extended the by adding, apart from further cell species, also further networks with prescribed properties, such as allowing for possible degradation, by adding a further phase-field variable into the formulation. Similarly, one can add another (non-conserved) component to model the network fibers that are secreted by the cells and thus allow for remodeling of the hydrogel. In addition, further properties such as phase separation into regions of high and low fiber concentration induced by cell traction forces can be included. The systematic extensions of the model framework and their predictions form the basis for future validation by in vitro experimental work in order to gain a fundamental understanding of the intricate mechanical interplay between cells and the ECM in tissue formation.

We analyzed the geometrical set-up of a clamped rectangular layer for which we investigated the stress–strain state by applying specific loads at the clamped boundaries, leaving the other boundaries free. We compared scenarios that also allow for possible exchange of the solvent through the free boundaries. In addition we compared our results for the neo-Hooke and the Gent model for the nonlinear elastic network to determine the effects of strain-stiffening on pattern formation of the cell population. Using the stress–strain relationship, it can be demonstrated that Gent-type materials are strain-stiffening, while neo-Hookean materials exhibit strain-softening behavior. Moreover, the stress–strain relationship for hydrogels under plane stress condition with constant solvent concentration barely differs from that of a pure elastic material. However, this changes in the approximation for plane strains. In addition, if solvent flow into or out of the hydrogel is allowed, the stress–strain relationship and the stiffness of the material also differ significantly from that of a pure elastic material under plane stress condition. In this paper we have focused on 2D approximations and have not taken into account the possibility of 3D effects such as wrinkling, which has been extensively studied for pure elastic sheets, which is ongoing research.

Turning towards cell migration and orientation on stretched hydrogel layers, one initially recognizes expected behavior, i.e. cells orient themselves vertically, in the direction of stretch under small applied strain. However, for large enough applied strain, the orientation of the cells undergoes a transition in the horizontal direction, which is interesting in particular for the Gent-type case, since alignment with the direction of the stretch would be expected for strain-stiffening materials, cf. [12]. Our choice for the ABM prefers horizontal alignment for cells interacting with a hydrogel layer subject to sufficiently large external loading, because of how we have defined the deformation function. This suggests adapting this function to the case of external loading. We note that for sufficiently large external load, the lateral deformation $|F_{xx} - 1|$ is smaller than the vertical one $|F_{yy} - 1|$ for both neo-Hookean and Gent type materials and in particular for the non-conserved case. In addition, biological cells constantly reattach to the ECM and therefore measure changes in the deformation relative to an external field, i.e. the stiffness being the second derivative of the energy density.

Moreover, at higher strains for non-conserved hydrogels under plane-stress conditions, we observe a change in the shape of the Gent hydrogel compared to the neo-Hookean one, which in turn affects cell migration. While the Gent-type hydrogel reduces its volume by squeezing solvent out of the sheet, the neo-Hookean hydrogel expands in volume as solvent flows into the material. In the case of the Gent hydrogel, the cells migrate towards the clamped boundaries and the formation of cell chains is suppressed. In the neo-Hookean model, on the other hand, the cells form horizontal long-range alignments that are distributed over the entire length of the stretched thin sheet.

In conclusion, the mathematical framework presented in this work provides a versatile toolbox to model complex processes that affect the cellular motility. We used stressed hydrogel sheets to benchmark cell behavior. The true strength of this framework lies in extensibility, e.g. the inclusion of solvents will allow for the integration of intricate biological processes such as biochemical signaling or cellular responses or ECM remodeling in the future.

Acknowledgements AE and LS were supported by the German Research Foundation (DFG) under Germany's Excellence Strategy - MATH$^+$: The Berlin Mathematics Research Center (EXC-2046/1 - project ID: 390685689) via the project AA1-12*. We acknowledge financial support by the DFG Priority Program SPP 2171 *Dynamic Wetting of Flexible, Adaptive, and Switchable Substrates* within the projects 422786086 (LS, AE) and 422792530 (DP). CD was supported by the DFG through the Collaborative Research Centre (CRC) 1444, project ID: 427826188.

Funding Open Access funding enabled and organized by Projekt DEAL. The fund was granted by Deutsche Forschungsgemeinschaft (Grant Nos. CRC 1444, project ID: 427826188, MATH+: EXC-2046/1, project ID: 390685689, SPP 2171, project ID: 422786086, SPP 2171, project ID: 422792530.

References

1. Lee KY, Mooney DJ (2012) Alginate: properties and biomedical applications. Prog Polym Sci 37:106–126
2. Hopkins AM et al (2013) Silk hydrogels as soft substrates for neural tissue engineering. Adv Func Mater 23:5140–5149. https://doi.org/10.1002/adfm.201300435
3. Mousavi SJ, Doweidar MH (2019) Encapsulated piezoelectric nanoparticle-hydrogel smart material to remotely regulate cell differentiation and proliferation: A finite element model. Comput Mech 63:471–489
4. Gaziano P, Marino M (2023) A phase-field model of cell motility in biodegradable hydrogel scaffolds for tissue engineering applications. Comput Mech 74:1–22
5. Janmey PA, Winer JP, Weisel JW (2009) Fibrin gels and their clinical and bioengineering applications. J R Soc Interface 6:1–10
6. Borgiani E, Duda GN, Checa S (2017) Multiscale modeling of bone healing: toward a systems biology approach. Front Physiol 8:287
7. Hogrebe NJ, Reinhardt JW, Gooch KJ (2017) Biomaterial microarchitecture: a potent regulator of individual cell behavior and multicellular organization. J Biomed Mater Res, Part A 105:640–661
8. Brauer E et al (2019) Collagen fibrils mechanically contribute to tissue contraction in an in vitro wound healing scenario. Advanced Science 6:1801780
9. Checa S, Rausch MK, Petersen A, Kuhl E, Duda GN (2015) The emergence of extracellular matrix mechanics and cell traction forces as important regulators of cellular self-organization. Biomech Model Mechanobiol 14:1–13
10. Checa S, Prendergast PJ (2009) A mechanobiological model for tissue differentiation that includes angiogenesis: a lattice-based modeling approach. Ann Biomed Eng 37:129–145
11. Abdalrahman T, Checa S (2022) On the role of mechanical signals on sprouting angiogenesis through computer modeling approaches. Biomech Model Mechanobiol 21:1623–1640. https://doi.org/10.1007/s10237-022-01648-4
12. Ahearne M (2014) Introduction to cell-hydrogel mechanosensing. Interface Focus 4:20130038
13. Talebian S et al (2019) Self-healing hydrogels: the next paradigm shift in tissue engineering? Advanced Science 6:1801664
14. Mandal A, Clegg JR, Anselmo AC, Mitragotri S (2020) Hydrogels in the clinic. Bioengineering & Translational Medicine 5:e10158. https://doi.org/10.1002/btm2.10158
15. Noor N et al (2019) 3d printing of personalized thick and perfusable cardiac patches and hearts. Advanced Science 6:1900344
16. Peña B et al (2018) Injectable hydrogels for cardiac tissue engineering. Macromol Biosci 18:1800079
17. Bertsch P, Diba M, Mooney DJ, Leeuwenburgh SCG (2023) Self-healing injectable hydrogels for tissue regeneration. Chem Rev 123:834–873
18. Liu T et al (2024) Advanced cardiac patches for the treatment of myocardial infarction. Circulation 149:2002–2020
19. Caccavo D, Cascone S, Lamberti G, Barba A (2018) Hydrogels: experimental characterization and mathematical modelling of their mechanical and diffusive behaviour. Chem Soc Rev 47:2357–2373
20. Solbu AA et al (2022) Assessing cell migration in hydrogels: An overview of relevant materials and methods. Materials Today Bio 100537
21. Hazur J, Endrizzi N, Schubert DW, Boccaccini AR, Fabry B (2022) Stress relaxation amplitude of hydrogels determines migration, proliferation, and morphology of cells in 3-D culture. Biomaterials Science 10:270–280
22. Chaudhuri O (2017) Viscoelastic hydrogels for 3D cell culture. Biomaterials Science 5:1480–1490
23. Münster S et al (2013) Strain history dependence of the nonlinear stress response of fibrin and collagen networks. Proc Natl Acad Sci 110:12197–12202. https://doi.org/10.1073/pnas.1222787110
24. Wang JH, Grood ES (2000) The strain magnitude and contact guidance determine orientation response of fibroblasts to cyclic substrate strains. Connect Tissue Res 41:29–36
25. Isomursu A et al (2022) Directed cell migration towards softer environments. Nat Mater 21:1081–1090
26. Dazzi C et al (2023) External mechanical loading overrules cell-cell mechanical communication in sprouting angiogenesis during early bone regeneration. PLoS Comput Biol 19:1–27. https://doi.org/10.1371/journal.pcbi.1011647
27. Alisafaei F, Chen X, Leahy T, Janmey PA, Shenoy VB (2021) Long-range mechanical signaling in biological systems. Soft Matter 17:241–253
28. Natan S, Koren Y, Shelah O, Goren S, Lesman A (2020) Long-range mechanical coupling of cells in 3D fibrin gels. Mol Biol Cell 31:1474–1485
29. Liu K, Wiendels M, Yuan H, Ruan C, Kouwer PH (2022) Cell-matrix reciprocity in 3D culture models with nonlinear elasticity. Bioactive Materials 9:316–331
30. Wolf K et al (2009) Collagen-based cell migration models in vitro and in vivo. Seminars in Cell & Developmental Biology 20:931–941
31. Licup AJ et al (2015) Stress controls the mechanics of collagen networks. Proc Natl Acad Sci 112:9573–9578. https://doi.org/10.1073/pnas.1504258112
32. Haupert S, Guérard S, Mitton D, Peyrin F, Laugier P (2015) Quantification of nonlinear elasticity for the evaluation of submillimeter crack length in cortical bone. J Mech Behav Biomed Mater 48:210–219
33. Winer JP, Oake S, Janmey PA (2009) Non-linear elasticity of extracellular matrices enables contractile cells to communicate local position and orientation. PLoS ONE 4:e6382
34. Wen Q, Janmey PA (2013) Effects of non-linearity on cell-ECM interactions. Exp Cell Res 319:2481–2489

35. Grekas G et al (2021) Cells exploit a phase transition to mechanically remodel the fibrous extracellular matrix. J R Soc Interface 18:20200823
36. Reinhardt JW, Krakauer DA, Gooch KJ (2013) Complex matrix remodeling and durotaxis can emerge from simple rules for cell-matrix interaction in agent-based models. J Biomech Eng 135:071003
37. Borgiani E, Duda GN, Willie BM, Checa S (2021) Bone morphogenetic protein 2-induced cellular chemotaxis drives tissue patterning during critical-sized bone defect healing: an in silico study. Biomech Model Mechanobiol 20:1627–1644. https://doi.org/10.1007/s10237-021-01466-0
38. Perier-Metz C, Duda GN, Checa S (2021) Initial mechanical conditions within an optimized bone scaffold do not ensure bone regeneration—an in silico analysis. Biomech Model Mechanobiol 20:1723–1731. https://doi.org/10.1007/s10237-021-01472-2
39. Vernerey FJ, Lalitha Sridhar S, Muralidharan A, Bryant SJ (2021) Mechanics of 3d cell-hydrogel interactions: experiments, models, and mechanisms. Chem Rev 121:11085–11148
40. Dolbow J, Fried E, Ji H (2004) Chemically induced swelling of hydrogels. J Mech Phys Solids 52:51–84
41. Ji H, Mourad H, Fried E, Dolbow J (2006) Kinetics of thermally induced swelling of hydrogels. Int J Solids Struct 43:1878–1907
42. Drozdov AD, Papadimitriou A, Liely J, Sanporean C-G (2016) Constitutive equations for the kinetics of swelling of hydrogels. Mech Mater 102:61–73
43. Hennessy MG, Münch A, Wagner B (2020) Phase separation in swelling and deswelling hydrogels with a free boundary. Phys Rev E 101:032501
44. Rognes ME, Calderer M-C, Micek CA (2009) Modelling of and mixed finite element methods for gels in biomedical applications. SIAM J Appl Math 70:1305–1329
45. Yuan M, Chen W, Wang C, Wise SM, Zhang Z (2021) An energy stable finite element scheme for the three-component Cahn–Hilliard-type model for macromolecular microsphere composite hydrogels. J Sci Comput 87:78
46. Schmeller L, Peschka D (2023) Gradient flows for coupling order parameters and mechanics. SIAM J Appl Math 83:225–253
47. Chester SA, Anand L (2010) A coupled theory of fluid permeation and large deformations for elastomeric materials. J Mech Phys Solids 58:1879–1906
48. Drozdov A, Papadimitriou A, Liely J, Sanporean C-G (2016) Constitutive equations for the kinetics of swelling of hydrogels. Mech Mater 102:61–73
49. Huggins ML (1942) Theory of solutions of high polymers. J Am Chem Soc 64:1712–1719
50. Flory PJ (1942) Thermodynamics of high polymer solutions. J Chem Phys 10:51–61
51. Bosnjak N, Nadimpalli S, Okumura D, Chester SA (2020) Experiments and modeling of the viscoelastic behavior of polymeric gels. J Mech Phys Solids 137:103829
52. Kim B et al (2012) A comparison among Neo-Hookean model, Mooney-Rivlin model, and Ogden model for chloroprene rubber. Int J Precis Eng Manuf 13:759–764
53. Gent AN (1996) A new constitutive relation for rubber. Rubber Chem Technol 69:59–61
54. Jin L, Suo Z (2015) Smoothening creases on surfaces of strain-stiffening materials. J Mech Phys Solids 74:68–79
55. Holzapfel G (2001) Biomechanics of soft tissue, 1049–1063 (Academic Press, United States) volume iii, multiphysics behaviors, chapter 10, composite media edn
56. Dunn MG, Silver FH, Swann DA (1985) Mechanical analysis of hypertrophic scar tissue: structural basis for apparent increased rigidity. J Investig Dermatol 84:9–13
57. Imaoka C et al (2023) Inverse mechanical-swelling coupling of a highly deformed double-network gel. Sci Adv 9:eabp8351
58. Alnæs M et al (2015) The FEniCS project version 1.5. Arch Numer Softw 3
59. Logg A, Mardal K-A, Wells G (2012) Automated solution of differential equations by the finite element method: the FEniCS book, vol 84. Springer, Berlin
60. Erhardt AH, Peschka D, Schmeller L (2023) Modeling cellular self-organization in strain-stiffening hydrogels. https://github.com/andreerhardt/hydrogel_abm
61. Wong S, Guo W-H, Wang Y-L (2014) Fibroblasts probe substrate rigidity with filopodia extensions before occupying an area. Proc Natl Acad Sci 111:17176–17181
62. Kuboki T, Chen W, Kidoaki S (2014) Time-dependent migratory behaviors in the long-term studies of fibroblast durotaxis on a hydrogel substrate fabricated with a soft band. Langmuir 30:6187–6196
63. Hakkinen KM, Harunaga JS, Doyle AD, Yamada KM (2011) Direct comparisons of the morphology, migration, cell adhesions, and actin cytoskeleton of fibroblasts in four different three-dimensional extracellular matrices. Tissue Eng Part A 17:713–724
64. Trichet L et al (2012) Evidence of a large-scale mechanosensing mechanism for cellular adaptation to substrate stiffness. Proc Natl Acad Sci 109:6933–6938
65. Peng Q (2021) Mathematical aspects of cell-based and agent-based modelling for skin contraction after deep tissue injury. Ph.D. thesis, Delft University of Technology
66. Westman AM, Peirce SM, Christ GJ, Blemker SS (2021) Agent-based model provides insight into the mechanisms behind failed regeneration following volumetric muscle loss injury. PLoS Comput Biol 17:1–29. https://doi.org/10.1371/journal.pcbi.1008937
67. Steinwachs J et al (2016) Three-dimensional force microscopy of cells in biopolymer networks. Nat Methods 13:171–176
68. Koppl T, Wohlmuth B (2014) Optimal a priori error estimates for an elliptic problem with dirac right-hand side. SIAM J Numer Anal 52:1753–1769
69. Pablo AJ, Garau Eduardo M, Pedro M (2014) A posteriori error estimates for elliptic problems with dirac measure terms in weighted spaces. ESAIM: M2AN 48:1557–1581. https://doi.org/10.1051/m2an/2014010
70. Cerda E, Mahadevan L (2003) Geometry and physics of wrinkling. Phys Rev Lett 90:074302
71. Van Helvert S, Friedl P (2016) Strain stiffening of fibrillar collagen during individual and collective cell migration identified by AFM nanoindentation. ACS Applied Materials & Interfaces 8:21946–21955
72. Jaspers M et al (2014) Ultra-responsive soft matter from strain-stiffening hydrogels. Nat Commun 5:1–8
73. Jaspers M et al (2017) Nonlinear mechanics of hybrid polymer networks that mimic the complex mechanical environment of cells. Nat Commun 8:1–10
74. Steinwachs J (2015) Cellular Forces during Migration through Collagen Networks (Friedrich-Alexander-Universitaet Erlangen-Nuernberg (Germany))
75. Cóndor M et al (2019) Breast cancer cells adapt contractile forces to overcome steric hindrance. Biophys J 116:1305–1312
76. Elosegui-Artola A (2021) The extracellular matrix viscoelasticity as a regulator of cell and tissue dynamics. Curr Opin Cell Biol 72:10–18